Energetics of (super)tidal baroclinic modes in a realistically forced global ocean simulation

Maarten C. Buijsman[1], Mujeeb Abdulfatai[1], Brian K. Arbic[2], Eric P. Chassignet[3], Luna Hiron[3], Jay F. Shriver[4], Miguel Solano[5], Dheeraj Varma[1], Xiaobiao Xu[3]

[1]School of Ocean Science and Engineering, University of Southern Mississippi, 1020 Balch Blvd, Stennis Space Center, MS 39529, United States
[2]Department of Earth and Environmental Sciences, University of Michigan, 428 Church St, Ann Arbor, MI 48109, United States
[3]Center for Ocean-Atmospheric Prediction Studies, Florida State University, 2000 Levy Ave 292, Tallahassee, FL 32310, United States
[4]Naval Research Laboratory, 1005 Balch Boulevard, Stennis Space Center, MS 39529, United States
[5]Sofar Ocean, 28 Pier Annex, San Francisco, CA 94105, United States

Key Points:

- The energetics of internal wave modes are diagnosed for the diurnal, semidiurnal, and supertidal frequency bands.
- Low-mode supertidal energy is elevated in the tropics, in agreement with theory on resonant wave-wave interactions.
- The number of resolved diurnal ($\gtrapprox 6$), semidiurnal ($\sim$4), and supertidal ($\sim$2) modes is dictated by the horizontal grid spacing of 1/25°

Corresponding author: Maarten C. Buijsman , `maarten.buijsman@usm.edu`

Abstract

In this study, we diagnose the spatial variability in the energetics of tidally generated diurnal, semidiurnal, and supertidal internal wave vertical modes (up to mode 6) in a 30-day forward global ocean model simulation with a 4-km grid spacing and 41 layers. This simulation is forced with realistic tides and atmospheric fields. While diurnal modes are mostly generated in the western Pacific, semidiurnal modes are more ubiquitous in the global ocean. Supertidal modes are mostly generated at low latitudes. For all frequency bands, most of the energy is in mode 1. Diurnal modes are fully resolved beyond mode 6, semidiurnal modes are fully resolved up to mode 4, and supertidal modes are fully resolved up to mode 2, in agreement with a canonical horizontal resolution criterion. The meridional trends in the kinetic to available potential energy ratios of these resolved modes agree with an internal wave consistency relation. The supertidal band is dominated by the higher harmonics of the diurnal and semdiurnal tides, of which the terdiurnal and quarterdiurnal mode-1 waves have the most energy. Terdiurnal modes are mostly generated in the west Pacific, where diurnal internal tides are strong. In contrast, quarterdiurnal modes occur at all longitudes near strong semidiurnal generation sites. The consistency relation and frequency-wavenumber spectra show that the resolved supertidal modes are dispersive internal waves. These waves are likely generated by near-resonant interactions between tidal modes of the same mode number, which are enhanced in the tropics.

Plain Language Summary

In the density stratified oceans, internal waves propagate as disturbances along the density interfaces, with buoyancy as their restoring force. Due to the presence of the surface and seafloor, they form standing waves in the vertical and propagating waves in the horizontal. These waves are referred to as modes. Internal wave modes are generated by the tides, wind, and mean flows and can propagate for 1000s of kilometers. Because they carry substantial energy, their eventual dissipation contributes to watermass mixing. This mixing is important for maintaining the global ocean overturning circulation and the earth's climate. Hence, understanding the internal wave lifecycle in numerical ocean simulations is paramount. In this study, we compute the energy in the resolved internal wave modes in the diurnal, semidiurnal, and supertidal frequency bands in a realistically forced global ocean model simulation with a 4-km grid spacing and 41 layers. We verify that the horizontal grid spacing determines the resolution of the modes. The supertidal modes are dominated by the terdiurnal and quarterdiurnal waves. Their energy is elevated at the equator, most likely due to nonlinear interactions between waves with the same or differing tidal frequencies, but with the same mode number.

1 Introduction

With the availability of more powerful computing resources, the horizontal and vertical grid spacing of global ocean circulation models that include tidal forcing continues to increase (Arbic et al., 2018; Arbic, 2022). As a consequence, these models have been able to better resolve the internal wave spectrum (e.g., Simmons et al., 2004; Arbic et al., 2004; Shriver et al., 2012; Müller et al., 2012; Müller et al., 2015; Rocha et al., 2016; Savage et al., 2017; Yu et al., 2019; Li & von Storch, 2020; Buijsman et al., 2020; Arbic et al., 2022; Xu et al., 2022). While many of these model studies focus on the tidal band or the Garrett-Munk spectrum (e.g., Garrett & Munk, 1975), the energy peaks that occur at the higher harmonics of the primary tidal frequencies, referred to as the supertidal band (> 2.5 cycles per day), have not received as much attention. In this paper, we evaluate how much supertidal energy projects on vertical modes in a realistically forced global HYbrid Coordinate Ocean Model simulation (HYCOM; Bleck, 2002; Chassignet et al., 2003, 2009) with 4-km horizontal grid spacing and 41 layers and discuss the mechanisms that drive energy to these supertidal wave modes.

Internal gravity waves can be decomposed into orthogonal vertical modes, which are a solution of the well-known Stürm-Liouville eigenvalue problem (Gill, 1982). From local buoyancy frequency vertical profiles, the Stürm-Liouville equation is solved for the eigenfunctions and eigenspeeds. Characteristics of these modes are an increase of the number of zero crossings of the vertical and horizontal velocity eigenfunctions, an increase of the horizontal wavenumber, and a decrease of the eigenspeed for increasing mode number. The solutions of this eigenvalue problem have been used to gain insight in the propagation of internal gravity waves and their interactions with topography and the slowly varying background flows (e.g., Zilberman et al., 2009; Buijsman et al., 2010; Kelly et al., 2012; Zhao et al., 2016; Kelly & Lermusiaux, 2016; Kelly, 2016; Buijsman et al., 2020; Gong et al., 2021; Kelly et al., 2021; Pan et al., 2021; Raja et al., 2022; Siyanbola et al., 2024). While modal energetics in global ocean simulations have been computed for tidal internal waves (internal tides, e.g., Buijsman et al., 2020; Kelly et al., 2021) and near-inertial waves (e.g., Simmons & Alford, 2012; Raja et al., 2022), the global energetics of supertidal internal gravity wave modes in global ocean simulations are not well studied.

Whereas interactions between internal waves and eddies and interactions between near-inertial waves also contribute to the filling out of the internal wave spectrum (e.g., Yang et al., 2023; Delpech et al., 2024; Barkan et al., 2024; Skitka et al., 2024), this study mainly focuses on the higher harmonic wave modes that result from near-resonant interactions of tidal internal wave modes. Offshore of strong internal tide generation sites, the supertidal signal in observations and model simulations is often dominated by the higher harmonics of the primary tidal forcing frequencies. For example, Solano et al. (2023) diagnosed kinetic energy spectra offshore of the Amazon shelf in a 1/25° global HYCOM simulation and found that the supertidal energy is mostly concentrated in the higher harmonics of the semidiurnal (D_2) tide, i.e., D_4, D_6, D_8, etc., (their Figure 1). Similarly, Tchilibou et al. (2022) also observed higher harmonics in a 1/36° regional model simulation offshore the Amazon shelf (their Figure 12). The strong D_2 internal tide generation in the Bay of Biscay also coincides with observations (van Haren et al., 2002; van Aken et al., 2007; van Haren & Maas, 2022) and model simulations (Pichon et al., 2013) of deep open ocean currents that have energy at the higher harmonic frequencies of D_2. In the South China Sea, the strong diurnal (D_1) internal tides interact with the D_2 internal tides to create odd harmonics at terdiurnal (D_3) and higher frequencies in mooring observations (Xie et al., 2010). Global drifter observations (Yu et al., 2019) and model simulations (Arbic et al., 2022) of near-surface kinetic energy also reveal that these higher harmonics are ubiquitous, albeit they are less-well defined in the observations than in the simulations.

Several mechanisms contribute to energy transfers to higher harmonic frequencies. These mechanisms are characterized by wave-wave or self-interactions and result from the advective terms in the Navier Stokes equations. For example, these interactions occur along internal wave beams when they interact with boundaries and stratification (Tabaei et al., 2005; Gerkema, 2006; Grisouard et al., 2011; Diamessis et al., 2014; Dauxois et al., 2018). Downscale energy transfers may also occur due to interactions between internal wave modes (Thorpe, 1966; Sutherland, 2016; Wunsch, 2017; Varma & Mathur, 2017; Varma et al., 2020). Sutherland (2016), Wunsch (2017), and Wunsch & Marcellino (2023) showed that nonlinear self-interaction of internal tide modes in non-uniform stratification results in energy being transferred to superharmonic disturbances forced at twice the horizontal wavenumber and frequency of the parent mode. An internal wave mode with a sufficiently large amplitude may trigger a 'superharmonic cascade' (Baker & Sutherland, 2020; Sutherland & Dhaliwal, 2022). In this cascade, successive superharmonics grow through wave-wave interactions to non-negligible amplitudes. The phase relationship between the superharmonics is such that when superimposed, the internal tide transforms into a series of short waves, e.g., solitary waves. This process is also referred to as nonlinear steepening.

Independent from each other, and published at the same time, studies by Wunsch & Marcellino (2023) and Solano et al. (2023) confirmed that the fraction of higher harmonic energy is enhanced in the tropics. Wunsch & Marcellino (2023) showed theoretically that resonant self-interactions between semidiurnal mode-1 waves are enhanced in the tropics, mainly due to the small Coriolis parameter f. Solano et al. (2023) demonstrated that the fraction of baroclinic supertidal energy of the total tidal baroclinic energy is enhanced in the tropics in global model simulations. Gerkema & Zimmerman (1995) were among the first to show that the absence of rotation facilitated the disintegration of the internal tide into supertidal (solitary) waves. Semidiurnal internal tides are more susceptible to this nonlinear steepening than diurnal waves because the frequency of the former is closer to f (Farmer et al., 2009). Gerkema (2001) found that the disintegration of the mode-1 internal tide is strongest for surface intensified stratification, as occurs in the (sub)tropics (Kunze, 2017).

In this paper, we present a global modal decomposition for (super)tidal frequency bands. We project the modal eigenfunctions on the time varying 3D fields to extract time series of modal amplitudes for velocity and pressure, and compute the modal energetics. The research questions that we address in this paper are: 1) What is the spatial variability of the energetics of the (super)tidal modes? 2) What supertidal frequencies dominate and where? 3) What are the mechanisms that transfer energy from the tidal to these supertidal modes? 4) How does grid spacing affect the resolution of the (super)tidal modes?

In the remainder of this paper, in the Methods section, we discuss the global HYCOM simulation, the modal analysis, and energy diagnostics. In the Results section, we diagnose the modal energetics for several frequency bands and establish what supertidal frequencies are most important. In the fourth section we discuss how gridsize affects the number of resolved modes and the potential generation mechanisms of the supertidal modes. We end with conclusions.

2 Methods

2.1 Model

We use a global HYCOM simulation forced with tides and 3-hourly winds (expt_19.0), which has also been described in Raja et al. (2022) and Solano et al. (2023). The simulation has 41 hybrid layers and a tripole grid with a horizontal grid spacing of 1/25° (4 km at the equator). The hybrid grid comprises about ∼20 z-coordinate levels covering the surface mixed layer, isopycnal layers in the stratified interior, and terrain-following coordinates on the shelves. The thickness of the z-coordinate layers ranges from 1 m at the surface to 8 m near the bottom of the mixed layer. The depth of the deepest z coordinate varies globally and is about 100-200 m at low to mid latitudes. The model simulation is forced with five tidal constituents, i.e., M_2, S_2, N_2, O_1, and K_1. For the best tidal performance, a spatially varying self attraction and loading term in conjunction with a Kalman filter and a wave drag are applied (Ngodock et al., 2016). The simulation is initialized on 1 April 2019 from a simulation that is constrained by data assimilation (DA). It is run forward for about 50 days to allow transients associated with the DA (Raja et al., 2024) to dampen out. In this paper, we diagnose hourly 3D output over 30 days from 20 May to 19 June 2019. We perform our diagnostics for every other horizontal grid point to speed up our analyses and limit storage by a factor of four.

An older model simulation for September 2016 (expt_22.0) with the same set-up as expt_19.0 has shown to be in good agreement with M_2 surface and internal tide observations (Buijsman et al., 2020). For an overview of studies that have validated realistically-

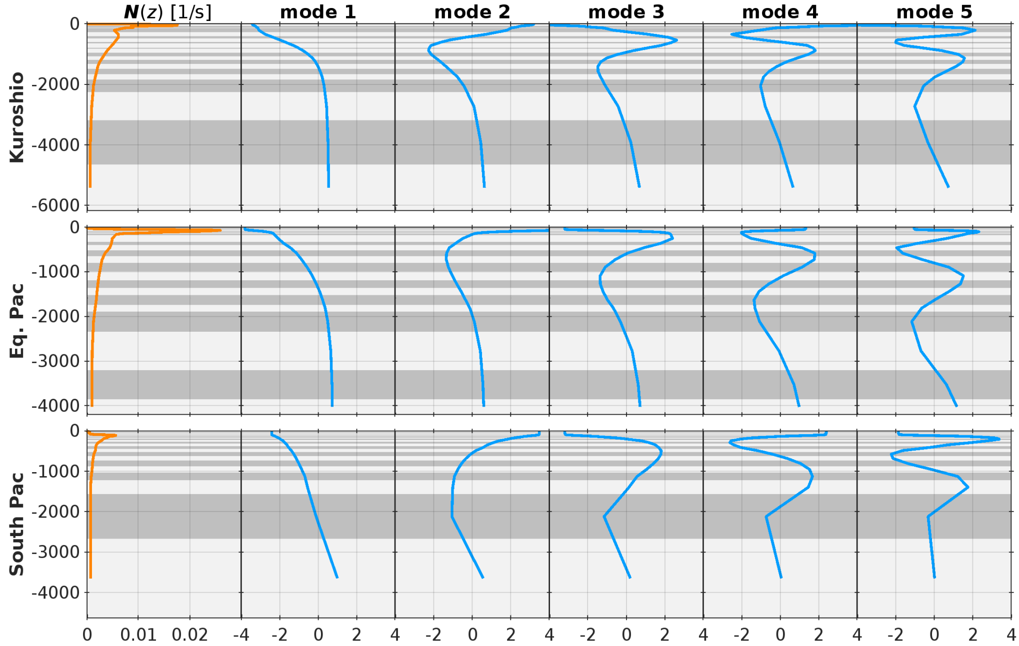

Figure 1. The buoyancy frequencies (first column) and the first five $\mathcal{U}_n$ eigenfunctions computed at three locations in the Pacific Ocean: a mid-latitude location (Kuroshio at 27.98°N and 150°E; top), the equator (Eq.Pac at 2.84°S and 228°E; middle), and the Southern Ocean (South Pac. at 66.85°S and 228°E; bottom). The time-mean layer thicknesses are alternately shaded with dark and light gray colors. The $\mathcal{U}$ eigenfunctions are unitless.

forced HYCOM simulations with observations over a range of frequencies, we refer to Arbic (2022).

2.2 Modes

Because our global simulation is hydrostatic, we solve the hydrostatic Stürm-Liouville eigenvalue problem

$$\frac{\partial^2 \mathcal{W}_n}{\partial z^2} + \frac{N^2}{c_n^2}\mathcal{W}_n = 0 \qquad (1)$$

for the first six modes for a 30-day time-mean and spatially varying buoyancy frequency $N(z)$, where $\mathcal{W}_n$ is the vertical velocity eigenfunction of mode n, c_n is the eigenspeed, and z is the vertical coordinate. Note that in the nonhydrostatic Stürm-Liouville equation, N^2 is replaced with $N^2 - \omega^2$, where ω is the internal wave frequency. In the hydrostatic eigenvalue problem, the eigenvalues and eigenfunctions do not depend on frequency. This allows us to project the eigenfunctions on the instantaneous fields.

Next we compute the horizontal velocity eigenfunction $\mathcal{U}_n = \partial \mathcal{W}_n / \partial z$ and normalize it so that $\frac{1}{H}\int_H \mathcal{U}_n^2 \mathrm{d}z = 1$, where H is seafloor depth (Buijsman et al., 2020). Examples of $N(z)$ and $\mathcal{U}_n$ for the first five modes near the Kuroshio, in the equatorial Pacific, and in the Southern Ocean are shown in Figure 1. The equatorial Pacific features the strongest surface intensified buoyancy frequency $N(z)$ and a more equal distribution of layer thicknesses in the deep ocean. Because of this relatively equal distribution, the higher modes are better resolved at depth, e.g., the curvature is realistic and the amplitudes between the zero-crossing are captured. In contrast, at the mid and higher latitudes the layer thickness distribution becomes more skewed with larger layer thick-

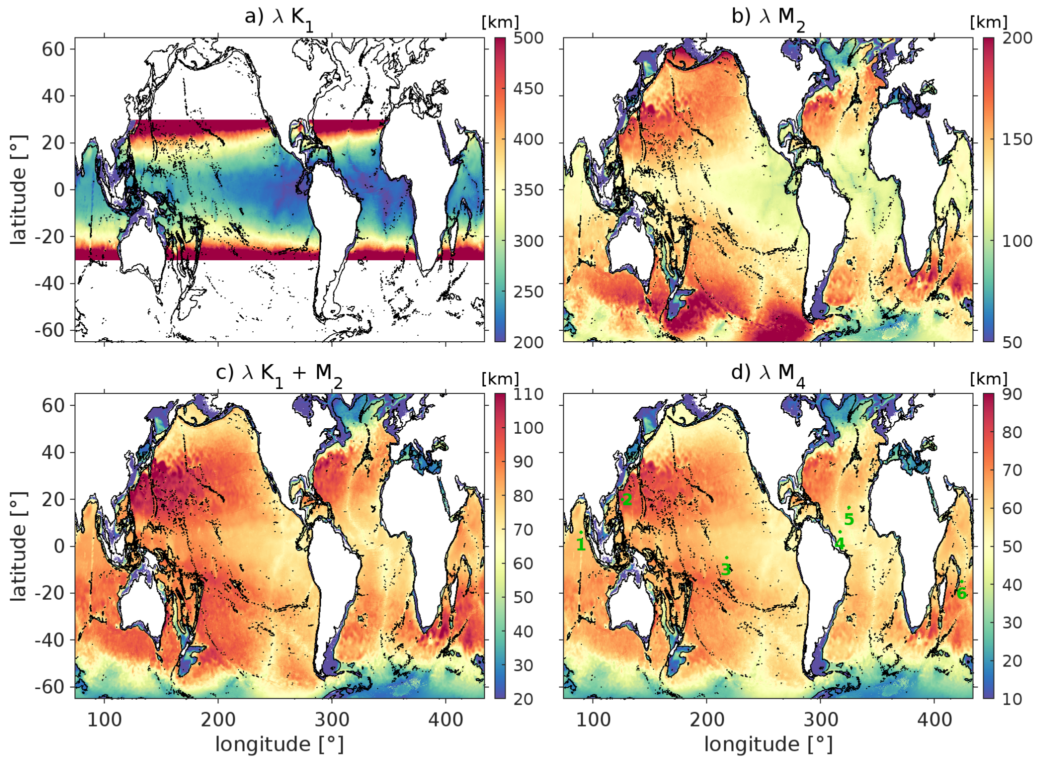

Figure 2. The mode-1 wavelengths for the (a) K_1, (b) M_2, (c) terdiurnal $K_1 + M_2$, and (d) quarterdiurnal M_4 internal tide frequencies. All colorbars have different scales. The numbers in (d) refer to the following geographic locations: (1) Bay of Bengal (5.94°N, 89.48°E), (2) Philippine Sea, east of Luzon Strait (20.06°N, 125.44°E), (3) Equatorial Pacific to the north of the French Polynesian islands (4.71°S, 217.2°E), (4) offshore the Amazon shelf (6.18°N, 316.88°E), (5) Cape Verde Basin (16.56°N, 324.84°E), and (6) to the east of the Mascarene Ridge (14.83°S, 424.12°E). Depth contours are shown at 0 and 2000 m.

nesses at depth. This causes higher modes to be less well resolved (e.g., modes 2-5 in the South Pacific in Figure 1).

Knowing c_n, we can compute the modal wavenumber k_n for a given frequency ω from the dispersion relation

$$\omega^2 = f^2 + k_n^2 c_n^2, \tag{2}$$

where f is the Coriolis frequency. As an example, we show the mode-1 wavelength $\lambda_1 = \frac{2\pi}{k_1}$ for diurnal (K_1), semidiurnal (M_2), terdiurnal (K_1+M_2), and quarterdiurnal (M_4) frequencies in Figure 2. The wavelength decreases for larger ω but it increases for larger f. In some locations at high latitudes ($> |\pm 50°|$), $N(z)$ becomes smaller and more depth-uniform, causing smaller c_n and smaller M_2, M_2+K_1, and M_4 wavelengths.

Next, we project the normalized horizontal velocity eigenfunctions on the 3D hourly time series of the HYCOM simulation to compute the modal amplitudes of the horizontal baroclinic velocities and perturbation pressures at each horizontal coordinate

$$\begin{aligned} \mathbf{u}(z,t) &= \Sigma_n \hat{\mathbf{u}}_n(t)\mathcal{U}_n(z), \\ p(z,t) &= \Sigma_n \hat{p}_n(t)\mathcal{U}_n(z), \end{aligned} \tag{3}$$

Table 1. Frequency range for the diurnal (D_1), semidiurnal (D_2), terdiurnal (D_3), quarterdiurnal (D_4), and supertidal (HH) bands, for which the energy terms are computed.

band σ	D_1	D_2	D_3	D_4	HH
ω range [cpd]	0.85-1.05	1.78-2.15	2.50-3.50	3.50-4.50	2.50-12.00

where $\mathbf{u} = (u, v)$ is the horizontal baroclinic velocity vector with velocities u and v along the x and y coordinates, respectively, p is the perturbation pressure, and $\hat{\mathbf{u}}_n(t)$ and $\hat{p}_n(t)$ are the modal amplitude time series for velocity and pressure, respectively. For further details on these calculations, the reader is referred to Buijsman et al. (2020) and Raja et al. (2022).

2.3 Modal Energetics

In contrast to previous studies (e.g., Buijsman et al., 2016; Raja et al., 2022; Solano et al., 2023), in which the modal amplitude time series were band-passed, we apply a Fast Fourier Transform to the time series, compute the energy terms, and sum over frequency bands. The advantage of this method is that it is faster and requires less memory. We first remove the linear trend in time from the modal amplitude time series and then apply a Tukey window with cosine fraction $\alpha = 0.2$ to minimize spectral leakage. We find that for $\alpha = 0.2$ the time-series variance is reduced by 7%. The results for $\alpha = 0.5$ are visually similar, while the variance is further reduced by 17%. We confirm that when the Tukey window is not applied, the spurious energy in the supertidal band is large at locations where subtidal energy is large, e.g., the Antarctic Circumpolar Current (ACC).

In a next step, we Fast Fourier Transform the modal amplitude time series, yielding complex coefficients as a function of frequency ω for velocity $\hat{\mathbf{u}}_n(\omega)$ and pressure $\hat{p}_n(\omega)$. For each mode number, we compute the time-mean modal kinetic energy integrated over tidal and supertidal frequency bands (Table 1) as

$$KE_{n,\sigma} = \rho_0 H \frac{1}{2m^2} \Sigma_\omega |\hat{\mathbf{u}}_n(\omega)|^2, \tag{4}$$

where m is the length of the time series and ρ_0 a reference density, and σ represents the frequency band. The time-mean modal available potential energy is computed as

$$APE_{n,\sigma} = \rho_0 H \frac{1}{2m^2} \Sigma_\omega \frac{|\hat{p}_n(\omega)|^2}{c_n^2 \rho_0^2}. \tag{5}$$

The time-mean modal pressure flux is computed as

$$\mathbf{F}_{n,\sigma} = H \frac{1}{2m^2} \Sigma_\omega \hat{\mathbf{u}}_n(\omega) \hat{p}_n^*(\omega), \tag{6}$$

where * is the complex conjugate. The reader is referred to Kelly et al. (2012) for details on the derivation of these energy terms.

3 Results

3.1 Energetics

3.1.1 Global Energy and Fluxes

The time-mean and depth-integrated modal kinetic energy and pressure fluxes for the D_1, D_2, and HH frequency bands are presented in Figures 3 and 4 for the first four modes. The spatial patterns of available potential energy are similar and are not shown.

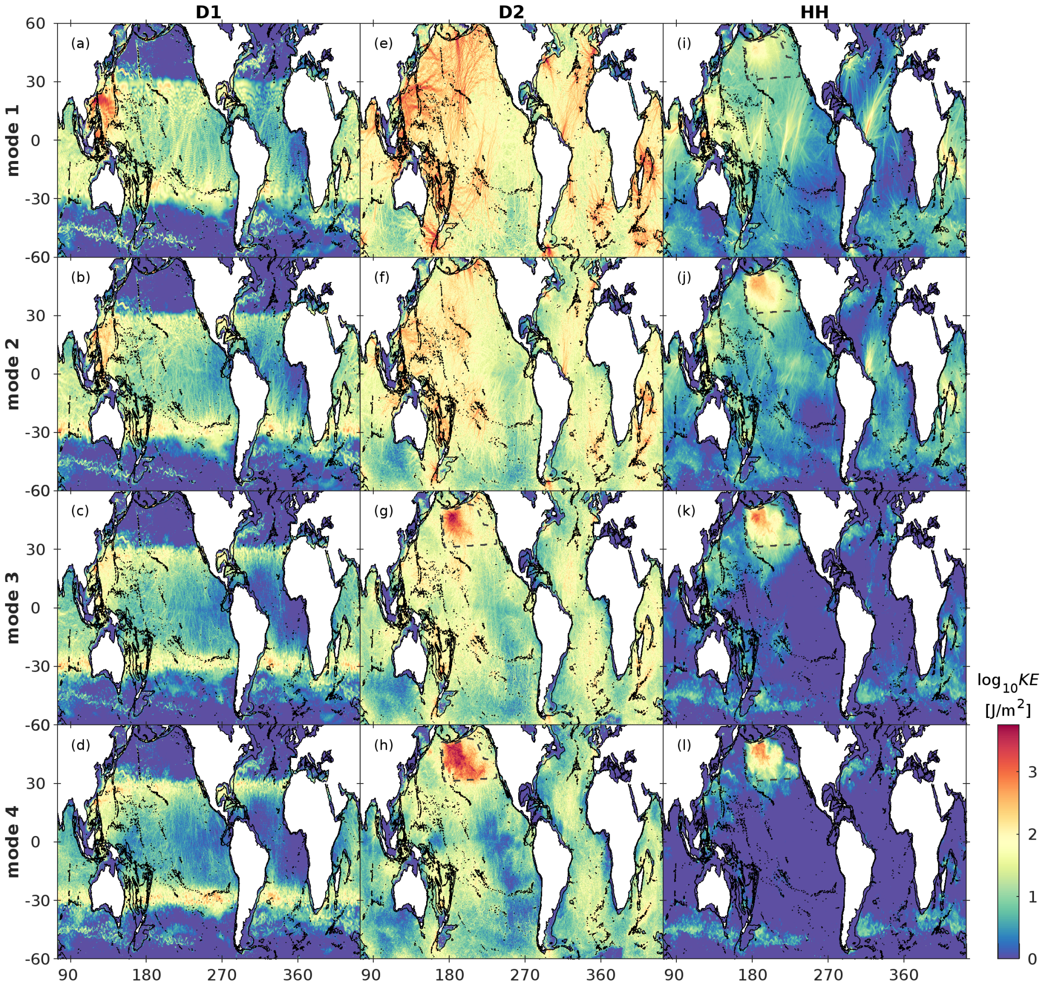

Figure 3. The time-mean and depth-integrated kinetic energy for the three frequency bands (columns) and modes 1 to 4 (rows). The dotted dark gray polygon in the north Pacific marks the extent of the thermobaric instabilities. Depth contours are shown at 0 and 2000 m.

Some subtle differences exist between the spatial patterns for $KE_{n,\sigma}$ and $|\mathbf{F}_{n,\sigma}|$. For diurnal modes near the diurnal turning latitudes ($\pm 30°$), near-inertial motions due to wind (e.g., Raja et al., 2022) and parametric subharmonic instabilities (PSI; e.g., Hazewinkel & Winters, 2011; Ansong et al., 2018) significantly enhance the kinetic energy of the higher modes (Figure 3), whereas the energy fluxes of the higher modes are much smaller as compared to mode 1 (Figure 4). This is because velocities and pressures are only correlated for propagating waves. Both the *KE* and energy flux of the semidiurnal modes 3 and higher and all supertidal modes are elevated due to thermobaric instabilities (TBI; Buijsman et al., 2020) in the north Pacific. TBI is a numerical noise that projects on modes with higher wavenumbers and frequencies. Recently, a solution that successfully mitigates TBI has been implemented (Alan Wallcraft, personal communication).

The strongest diurnal fluxes with magnitudes of $\mathcal{O}(10^4)$ W/m radiate southwest and southeastward from Luzon Strait (20.5°N and 121.4°E; Figure 4a-d). Smaller diurnal mode 1 fluxes of $\mathcal{O}(10^2)$ W/m appear to radiate equatorward from the diurnal turning latitudes near $\pm 30°$. Although some of these fluxes are from tidal origin, they can also be due to wind-generated near-inertial internal waves.

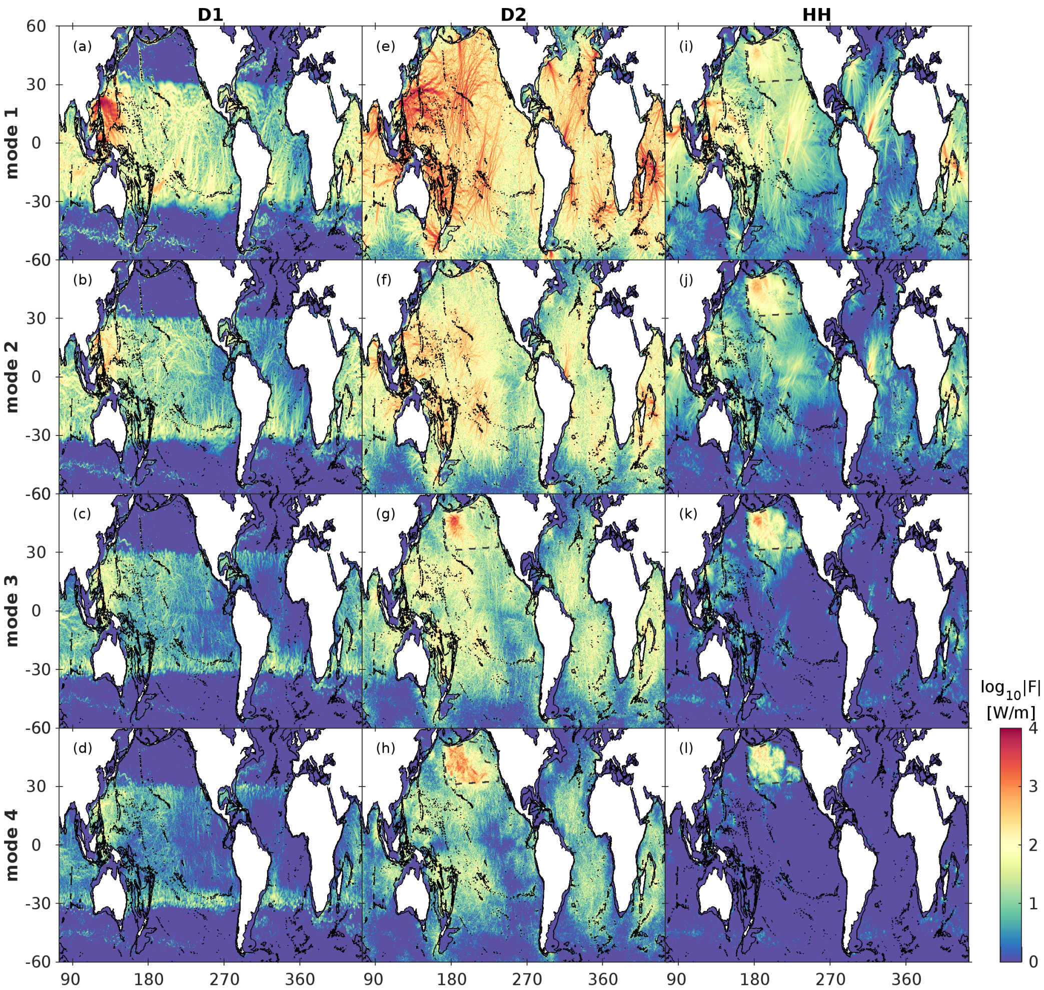

Figure 4. The same as Figure 3, but for the pressure flux magnitude.

In contrast to the diurnal energy flux, the semidiurnal energy flux is more equally distributed over the global ocean (Figure 4e-h). These fluxes are mostly attributed to the M_2 internal tide, which has been extensively discussed and validated in Buijsman et al. (2020). Moreover, semidiurnal high-mode fluxes are larger and more widespread than the diurnal high-mode fluxes. This may be because the most energetic diurnal internal tides are only generated in the northwest Pacific Ocean.

Supertidal fluxes in Figure 4i-l are largest for modes 1 and 2. The strongest supertidal fluxes of $\mathcal{O}(10^3)$ W/m occur near the equator in the Bay of Bengal, near Luzon Strait, offshore of the Amazon Shelf, and near the Mascarene Ridge (locations are marked in Figure 2). These supertidal beams coincide with strong mode-1 semidurnal internal tide beams (Figure 4e) that are generated at tall ridges and shelves.

3.1.2 Zonal Averages and Global Integrals

We area-average the depth-integrated *KE* and *APE* zonally over 10° latitude bins for seafloor depths $>$ 2000 m (Figure 5). Diurnal internal tides are dominant equatorward of $\pm 30°$, with the largest energy density at Luzon Strait near 20°N. While, near-inertial motions enhance modal *KE* in the diurnal band near the turning latitudes (Fig-

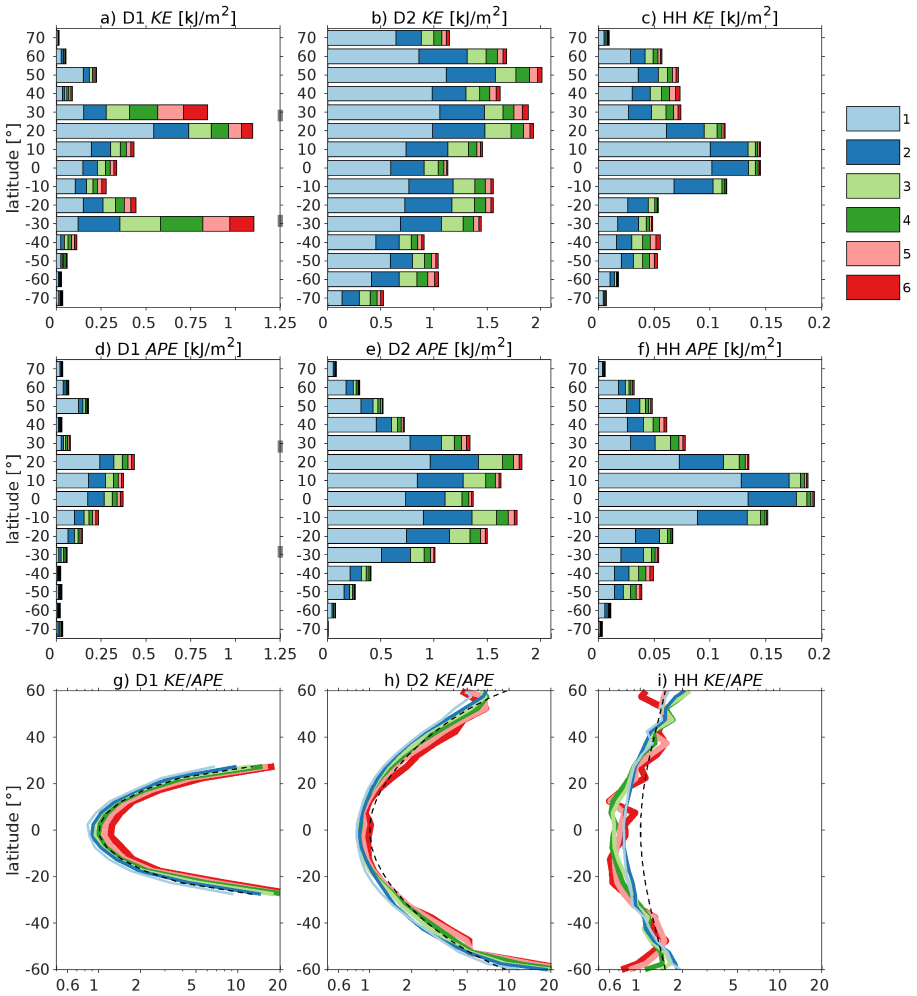

Figure 5. Zonally averaged (a-c) kinetic energy, (d-f) available potential energy, and (g-i) consistency relation $\frac{KE}{APE} = \frac{\omega^2+f^2}{\omega^2-f^2}$ for modes 1-6 and for the (a,d,g) diurnal, (b,e,h) semidiurnal, and (c,f,i) supertidal frequency bands. Energy is zonally averaged over 10° latitude bins for seafloor depths > 2000 m. The area with TBI has been excluded from the averages for the semidiurnal modes 3-6 and all supertidal modes. Where the diurnal-band frequencies overlap the local inertial frequencies, a thick grey line is added to the right axis in (a,d). In (g-i), $\frac{\omega^2+f^2}{\omega^2-f^2}$ is plotted as the dashed black line and the latitude range is limited because $\frac{KE}{APE}$ becomes noisy poleward of $|\pm 60°|$.

ure 5a), they do not affect diurnal *APE* (Figure 5d). For diurnal internal tides the mode 1 dominates, whereas the near-inertial kinetic energy is more equally distributed over all modes near ±30° (Raja et al., 2022). Poleward of ±30° only trapped diurnal modes exist, and energy levels are relatively low.

In accordance with Buijsman et al. (2020), the semidiurnal modal energy in Figure 5b,e is mostly tidal and dominated by mode 1, although higher modes (2-6) account for roughly half of the total energy. The simulated *KE* densities in Figure 5b are largest on the northern hemisphere, coinciding with large generation sites such as Georges Bank,

Table 2. Global integral of *KE* and *APE* per frequency band and modes 1-4 in PJ (= 10^{15} J) for seafloor depths > 250 m. The second column has the latitude range used for the global integral. Modal energy as a fraction of the energy summed over 6 modes (third column) is listed between parentheses in %. The area with TBI has been excluded from the integrals for the semidiurnal modes 3-6 and all supertidal modes. These values are affected by the Tukey window, which reduces the variance of each modal time series by ~7%. The area-integrated values are multiplied by a factor of four because only every grid point is stored.

KE	lat. range [°]	Σ_1^6	1	2	3	4
D_1	-30.0 to 30.0	28.1	9.5 (34)	6.0 (21)	4.1 (15)	3.5 (13)
D_2	-74.5 to 74.5	112.9	57.9 (51)	28.8 (26)	13.4 (12)	6.9 (6)
HH	-90.0 to 90.0	6.4	3.5 (55)	1.7 (27)	0.6 (9)	0.3 (5)
HH	-25.0 to 25.0	4.4	2.7 (63)	1.2 (27)	0.3 (7)	0.1 (2)
APE	lat. range [°]	Σ_1^6	1	2	3	4
D_1	-30.0 to 30.0	12.4	5.9 (47)	2.8 (23)	1.5 (12)	1.0 (8)
D_2	-74.5 to 74.5	85.7	45.5 (53)	21.9 (26)	10.1 (12)	4.7 (6)
HH	-90.0 to 90.0	7.4	4.2 (57)	2.0 (26)	0.7 (9)	0.3 (4)
HH	-25.0 to 25.0	5.6	3.5 (62)	1.5 (26)	0.4 (7)	0.1 (3)

Hawaii, and ridges in the northwestern Pacific, and decrease southward. In contrast, *APE* in Figure 5e is large at low latitudes and decreases towards the poles.

The supertidal *KE* and *APE* for modes 1-6 in Figure 5c,f show similar patterns, with the largest values occurring in the tropics. Interestingly, *APE* densities are larger than *KE* densities. Because these higher-frequency modes have shorter wavelengths, HH energy is only projected on modes 1 and 2.

Freely propagating waves satisfy the consistency relation

$$\frac{KE}{APE} = \frac{\omega^2 + f^2}{\omega^2 - f^2} \tag{7}$$

(Gill, 1982; Alford & Zhao, 2007; Nelson et al., 2020). To verify this in HYCOM, we compute the ratio of zonally averaged *KE* and *APE* for modes 1-6 and the D_1, D_2, and HH bands, and compare this with the theoretical ratio $\frac{\omega^2+f^2}{\omega^2-f^2}$ in Figure 5g-i. For all frequencies and modes, HYCOM correctly simulates the poleward increase of $\frac{KE}{APE}$ from ~1 at the equator in agreement with theory. This implies that these modes are propagating internal waves. However, the $\frac{KE}{APE}$ curves for D_2 modes 5-6 and HH modes 3-6 are noisier than the theoretical $\frac{\omega^2+f^2}{\omega^2-f^2}$. This suggests that these higher modes may not be well-resolved in our HYCOM simulation. Most of the resolved low modes are to the left of $\frac{\omega^2+f^2}{\omega^2-f^2}$. This implies that, consistently, *KE* is estimated too low or *APE* is estimated too high. Our estimate of *APE* (eq. 5) is a linearized form of *APE*, which omits higher order terms (Kang & Fringer, 2010). Possibly, this could contribute to our deviation from theory.

For comparison with the literature, we list the global integrals of modal *KE* and *APE* for seafloor depths > 250 m in Table 2. Mode 1 comprises roughly 50-60% of the energy summed over six modes for all bands except for the diurnal band, which contains more near-inertial high-mode energy. The total semidiurnal energy summed over the first six modes (199 PJ) is in agreement with Buijsman et al. (2020) (their Figure 9), after correcting for the contributions of the deep-water barotropic to baroclinic energy conversion of S_2 and N_2 (Egbert & Ray, 2003). The fraction of mode 1 supertidal energy

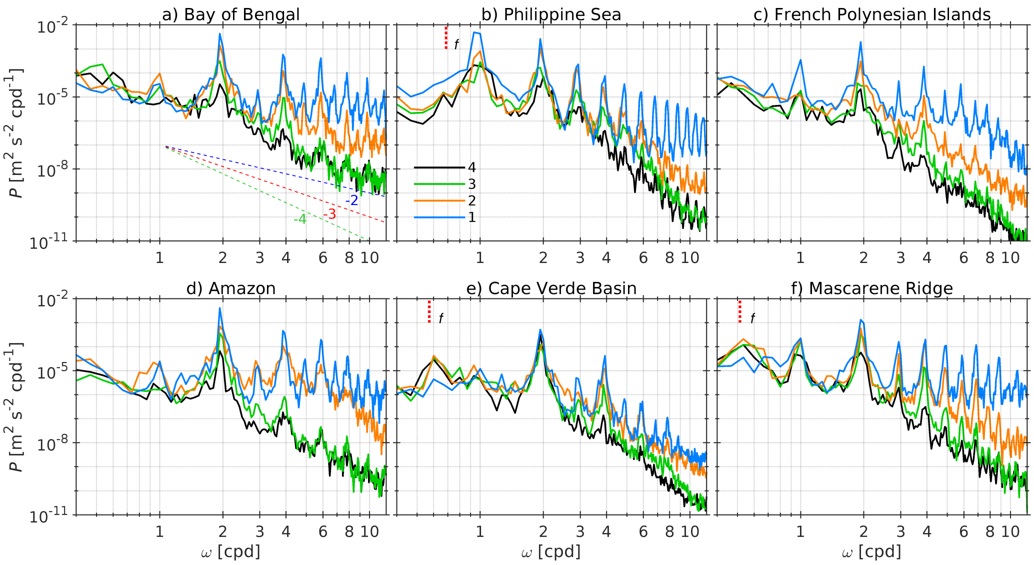

Figure 6. Kinetic energy spectra for modes 1-4 for six deep water sites: (a) Bay of Bengal (5.94°N, 89.48°E), (b) Philippine Sea, east of Luzon Strait (20.06°N, 125.44°E), (c) to the north of the French Polynesian islands (4.71°S, 217.2°E), (d) offshore the Amazon shelf (6.18°N, 316.88°E), (e) Cape Verde Basin, but in the Amazon beam (16.56°N, 324.84°E), and (f) to the east of the Mascarene Ridge (14.83°S, 424.12°E). All locations are marked in Figure 2. The diagonal dashed lines in (a) show ω^{-2}, ω^{-3}, and ω^{-4}. In all subplots, the vertical red dashed line marks the local inertial frequency.

of ∼60% is the largest equatorward of ±25°. The mode 1 supertidal energy comprises about 6% of the mode 1 semidiurnal energy (see also Solano et al., 2023).

3.2 Propagating Supertidal Modes

3.2.1 Frequency Spectra

A novel result of this paper is that we have decomposed the supertidal fields into vertical modes and quantified their energy content. Next, we investigate at what frequencies the supertidal energy is concentrated in our HYCOM simulation. We present *KE* spectra for the first four modes at six locations in the tropics in Figure 6. In addition to what is explained in Section 2.3, we compute these spectra for three 50% overlapping time-series windows to reduce noise.

In the beams radiating from the Andaman and Nicobar Islands in the Bay of Bengal (Figure 6a), the French Polynesian Islands in the equatorial Pacific (c), and the Amazon shelf (d and e) the supertidal mode 1 and 2 signals are dominated by the higher harmonics of D_2 (D_4, D_6, etc) because D_2 is the dominant tidal signal at these generation sites. In contrast, the supertidal energy of the beams radiating from Luzon Strait in the Philippine Sea (b) and from the Mascarene Ridge (f) is also dominated by the odd harmonics because diurnal tides are also important at these sites. At all sites, most of the supertidal energy is concentrated in modes 1 and 2, whereas the energy in the higher modes quickly drops off. Moreover, the higher modes have less distinct higher harmonic peaks.

The conclusions inferred from the spectra are reflected in the spatial maps of the mode 1 terdiurnal and quarterdiurnal *KE* in Figure 7a,b and their fractions of mode 1

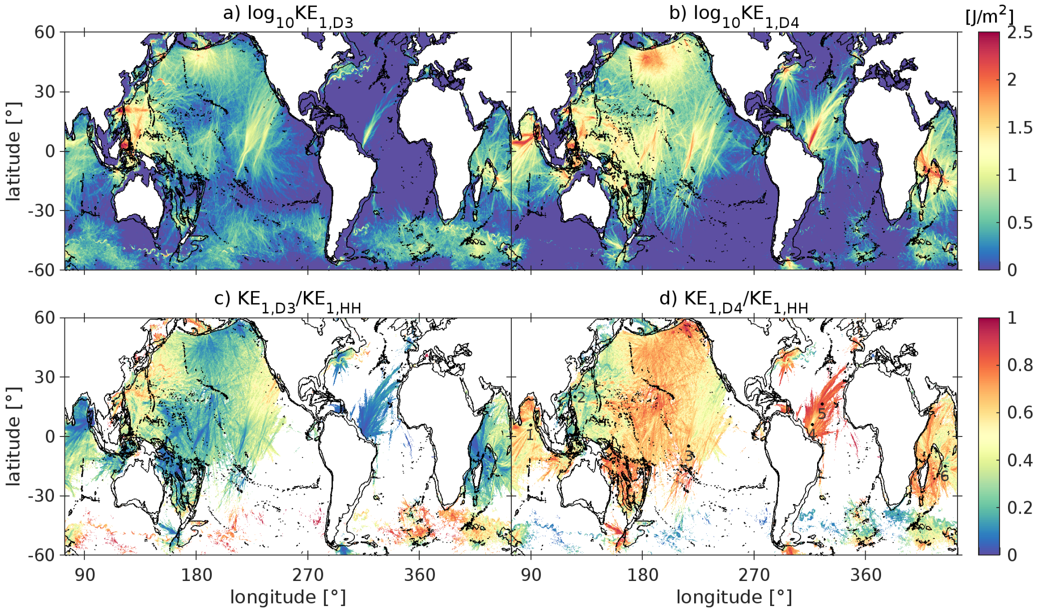

Figure 7. Mode 1 *KE* for the (a) D_3 and (b) D_4 frequency bands. Mode 1 *KE* for the (c) D_3 and (d) D_4 frequency bands normalized by mode 1 supertidal *KE*. In (c,d) areas with $KE_{1,\mathrm{HH}} < 5$ J/m^2 have been masked. The six locations of the spectra in Figure 6 are shown in (d) for convenience. Depth contours are shown at 0 and 2000 m.

supertidal *KE* in Figure 7c,d. The largest $KE_{1,\mathrm{D3}}$ and $KE_{1,\mathrm{D3}}/KE_{1,\mathrm{HH}}$ occur in the west Pacific near Luzon Strait and the Indonesian Archipelago, where D_1 is relatively large (Figure 3a). Here $KE_{1,\mathrm{D3}}/KE_{1,\mathrm{HH}}$ reaches values of 40-60% (Figure 7c). Outside this region, the supertidal band is dominated by D_4, with $KE_{1,\mathrm{D4}}/KE_{1,\mathrm{HH}}$ reaching values of about 80%. Interestingly, $KE_{1,\mathrm{D4}}/KE_{1,\mathrm{HH}}$ is higher in the farfield because the stronger nonlinearity in the nearfield causes the generation of more harmonics than only D_4. This can be clearly observed in the energy spectra along the beam generated at the Amazon shelf in Figure 6d,e.

3.2.2 Frequency-Wavenumber Spectra

The supertidal modes 1 and 2 that radiate from the major internal tide generation sites feature an unidirectional energy flux (Figure 4i,j). Moreover, their $\frac{KE}{APE}$ ratio follows the theoretical $\frac{\omega^2+f^2}{\omega^2-f^2}$ ratio (Figure 5i). This suggests that these modes are propagating internal waves. To further confirm this, we compute frequency-wavenumber spectra of steric sea-surface height along the nonlinear internal tide beams in the Bay of Bengal, the Philippine Sea, and offshore the Amazon shelf (Figure 8). The spectra are computed along the main internal tide beams. We remove the linear trends and apply a Tukey window in time and space and compute the spectra for three 50% overlapping time-series windows. The positive wavenumbers in Figure 8 represent waves radiating away from the main generation sites.

Echoing Figure 6, the Bay of Bengal and the Amazon beams are dominated by the harmonics of D_2, whereas the southeastward beam from Luzon Strait in the Philippine Sea has energy at the harmonics of both D_1 and D_2. At these three sites, the higher harmonics map onto the hydrostatic mode 1-3 dispersion curves (eqs. 1-2), confirming that the supertidal modes at these sites are indeed propagating internal waves. These results

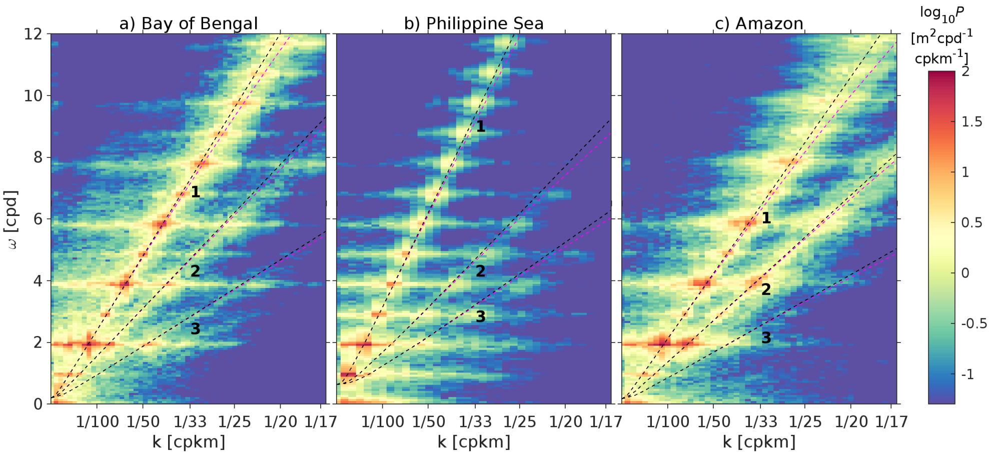

Figure 8. Frequency-wavenumber spectra of steric sea-surface height along the internal tide beams in (a) Bay of Bengal, (b) Philippine Sea, and (c) offshore the Amazon shelf. The $\omega - k$ spectra coincide with the locations of the frequency spectra of Figure 6. Energy is clearly elevated at the tidal harmonics and projects on the hydrostatic mode 1-3 dispersion curves (black dashed lines; eq. 2). For comparison, the nonhydrostatic dispersion curves are shown as magenta dashed lines. The dispersion curves represent the median over all k-values along the transect for the same ω.

raise the question: what mechanisms generate these propagating supertidal modes? We will discuss this in Section 4.2.1.

4 Discussion

4.1 Effect of Grid Spacing on the Resolution of Modes

The resolution of subtidal modes has been discussed in Hallberg (2013), Stewart et al. (2017), and Xu et al. (2023). While Buijsman et al. (2020) discusses the effect of horizontal grid spacing on semidiurnal modes, Hiron et al. (2024) discusses the effect of vertical grid spacing on tidal modes. In this section we briefly discuss the effect of horizontal and vertical grid spacing on resolving the dominant D_1, D_2, and D_4 vertical modes.

How well a mode is resolved in the horizontal depends on the number of gridcells per wavelength

$$\gamma = \frac{\lambda_n}{\tilde{\Delta}}, \tag{8}$$

where the effective horizontal grid spacing $\tilde{\Delta} = \sqrt{\frac{1}{2}(\Delta x^2 + \Delta y^2)}$ (Hallberg, 2013) and the horizontal grid spacings are Δx and Δy, which vary on the HYCOM tripole grid. γ should be larger than 2π to resolve propagating internal waves (Hallberg, 2013). In Appendix A, we consider how finite difference errors of a sinusoidal wave change as a function of the horizontal grid spacing. We compute amplitude errors of $17-10\%$ for $\gamma = 6-8$ grid cells per wavelength. We use this range as our horizontal resolution criterion to evaluate the number of modes resolved for the dominant K_1, M_2, and M_4 frequencies, representing the D_1, D_2, and HH frequency bands, respectively. The internal tide wavelengths in Figure 2, and thus also γ, feature larger meridional than zonal gradients. Hence, we average the maximum number of resolved modes over all longitudes and 10° latitude bins for seafloor depths > 2000 m (Figure 9). For both K_1 and M_2, the number of re-

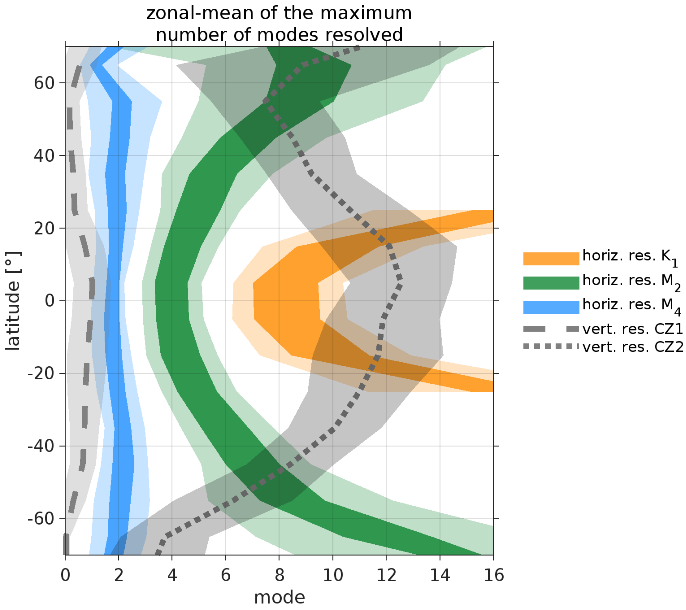

Figure 9. The maximum number of modes resolved for horizontal and vertical resolution criteria area-averaged over longitude and 10° latitude bins. The colored polygons indicate the number of resolved K_1 (orange), M_2 (green), and M_4 (blue) modes due to the horizontal grid spacing. The dark-colored polygons mark the extent of the zonal-mean values for $\gamma = 6$ and 8 and the light-colored polygons mark the extent of the zonal-mean values ± one standard deviation. The gray dashed lines mark the zonal-average for the vertical grid-spacing criteria CZ1, based on $\gamma \approx 2\pi$, and CZ2, based on 2 zero-crossings per HYCOM layer. The gray shaded polygons mark the extent of the zonal-mean values ± one standard deviation.

solved modes increases with latitude because λ_n increases for increasing f, whereas $\tilde{\Delta}$ decreases with latitude. In contrast, the maximum number of resolved modes for M_4 shows a much weaker latitudinal dependence.

In Figure 9 we also plot the maximum number of resolved modes for two vertical resolution criteria: CZ1 and CZ2. For CZ1 we assume a vertical mode is not resolved if the number of vertical layers between subsequent eigenfunction zero crossings is less than three ($\gamma \lesssim 2\pi$), in accordance with Stewart et al. (2017). According to this criterion, our HYCOM simulation barely resolves a mode-1 wave (Figure 9). In CZ2, we assume that a mode is not resolved when two $\mathcal{U}$ or two $\mathcal{W}$ zero-crossings occur in the same HYCOM layer. The deep isopycnal layers thickness in our HYCOM simulation increase from the equator to the poles (Figure 1), causing a polward decrease in the maximum number of resolved modes in Figure 9. In contrast to CZ1, CZ2 is generally less stringent than the horizontal resolution criterion for the three frequencies.

Do these horizontal and vertical resolution criteria correctly predict the maximum number of resolved propagating modes? Figures 3-5 indicate that for all three frequency bands more mode numbers contain energy than criterion CZ1 mandates. These results are in agreement with Xu et al. (2023), who showed that CZ1, which is really intended for z-coordinate models, is too strict for isopycnal layer models such as HYCOM. It can be inferred from Figures 3-5, that as the frequency increases and the wavelength decreases, fewer tidal modes are resolved. Ignoring near-inertial motions near ±30° latitude, D_1 has relatively more energy in mode 6 than the D_2 and HH modes. In the tropics, D_2 internal waves have most of their energy in modes 1-4, while HH waves have most of their energy in modes 1-2. The latter is clearly shown when considering the supertidal fluxes in Figure 4i,j. Beyond these mode numbers the energy quickly rolls off. The agreement with the consistency relation in Figure 5g-i also confirms this. These findings are in a reasonable agreement with the predicted number of resolved modes due to the horizontal grid spacing in the tropics (orange, green, and blue polygons in Figure 9), although the horizontal resolution criterion for K_1 predicts more resolved modes than the six modes we solve for. However, we do not find a clear correlation between the meridional trends in Figure 9 and the resolved modes (e.g., see Figure 5). For example, the poleward increase of the number of resolved M_2 modes due to the horizontal resolution to about $\pm 50°$ and a subsequent poleward decrease on the southern hemisphere mandated by the vertical resolution criterion CZ2 is difficult to discern from the energetics. This qualitative correlation may be adversely affected by how much energy is input into tidal modes when they are generated at topography in HYCOM, e.g., there may be energy input into fewer modes than the simulation can resolve according to our criteria.

4.2 Resonant Wave-Wave Interactions

4.2.1 Comparison with Theory

It is commonly accepted that the primary frequency internal tides are generated at topography (e.g., Vic et al., 2019; de Lavergne et al., 2019; Buijsman et al., 2020). In contrast, recent findings suggest that the low-mode supertidal internal waves are generated in the open ocean. For example, the generation of supertidal energy away from topography is clearly visible in the equatorial Pacific in Figures 4i and 7b. Solano et al. (2023) showed that the linear barotropic to baroclinic conversion at topography computed for the supertidal band cannot explain the positive supertidal flux divergence, which is large away from topography. They found that the positive supertidal flux divergence is largely explained by cross-frequency energy transfers from the tidal to the supertidal bands as determined with a coarse-graining approach (Aluie et al., 2018). Bell Jr. (1975) derived a topographic internal wave energy flux formulation, forced by the primary tidal frequencies, that includes contributions from the higher harmonics. However, it is yet to be determined how relevant the higher harmonic generation term in Bell's formulation is in ocean model simulations.

A likely candidate for the generation of the simulated higher harmonic internal waves (e.g., Figure 6) are (near-)resonant wave-wave interactions. Resonant wave-wave interactions may occur when the relations $\omega_a + \omega_b = \omega_c$ and $\mathbf{k}_a + \mathbf{k}_b = \mathbf{k}_c$ are satisfied (for an overview, see Lamb, 2007), where $\mathbf{k}$ is the wavenumber vector and subscripts a and b refer to the parent waves and subscript c refers to the resonant child wave. In theoretical studies, e.g., Wunsch (2017), Baker & Sutherland (2020), Sutherland & Dhaliwal (2022), and Wunsch & Marcellino (2023) studied the self interaction of a propagating mode 1 M_2 internal wave that generates a dispersive mode 1 M_4 internal wave. These harmonics may also interact with themselves and their parent waves, creating a superharmonic cascade that drives energy to smaller spatial and temporal scales (Sutherland & Dhaliwal, 2022). To determine where mode-1 M_2 self interactions may be resonant in the global ocean, Wunsch & Marcellino (2023) computed the resonance parameter

$$\epsilon = \frac{[\omega_a + \omega_b]^2 - [\omega(k_a + k_b)]^2}{[\omega_a + \omega_b]^2} \tag{9}$$

using realistic stratification inferred from Argo floats and the nonhydrostatic Stürm-Liouville equation. When ϵ is small, resonant wave-wave interactions may be enhanced. Wunsch & Marcellino (2023) showed that $1/\epsilon$ tends to infinity at the equator and decreases to zero polewards (their Figure 3). This meridional trend is mostly determined by the change in f with latitude. In a not-yet peer reviewed study, Baker et al. (2024) demonstrated that the double harmonic of M_2 can grow to non-negligible amplitudes in a few days when

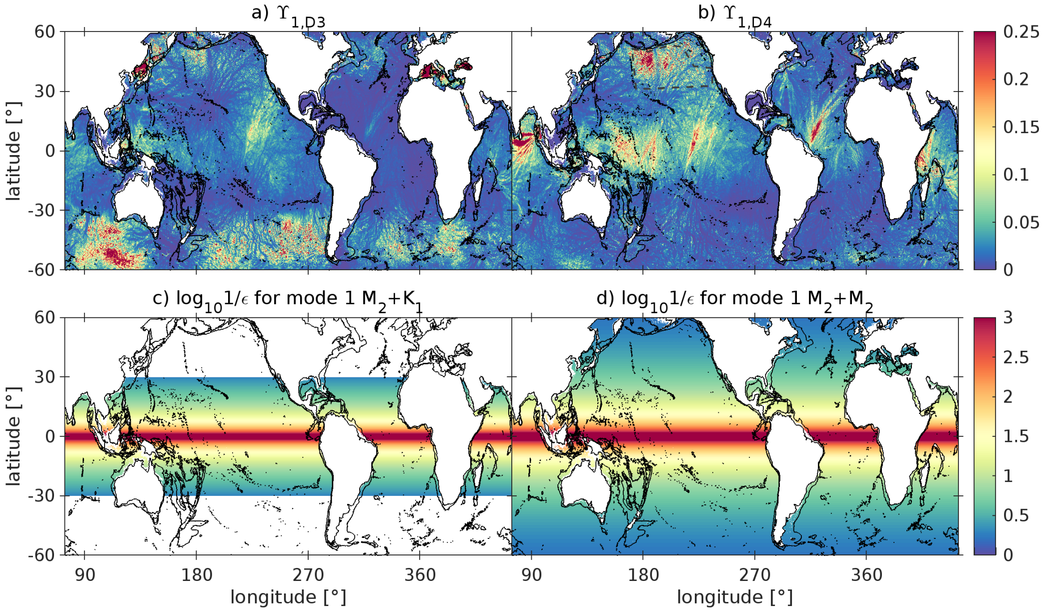

Figure 10. The ratio between mode 1 (a) terdiurnal and tidal KE, $\Upsilon_{1,\mathrm{D3}}$, and (b) quarter-diurnal and tidal KE, $\Upsilon_{1,\mathrm{D4}}$. Hydrostatic resonance parameter $1/\epsilon$ (eq. 12) for the interaction between mode 1 (c) $\mathrm{M_2}$ and $\mathrm{K_1}$ waves and (d) $\mathrm{M_2}$ and $\mathrm{M_2}$ waves. The area where TBI occurs is marked by the grey dashed line. Depth contours are shown at 0 and 2000 m.

ϵ is small near the equator. In agreement with these findings, Solano et al. (2023) showed that the supertidal baroclinic kinetic energy, not decomposed into modes, as a fraction of the total baroclinic tidal energy in a global HYCOM simulation is enhanced in the tropics (their Figure 2d). The correlation between theory and these model results suggests that near-resonant low-mode wave-wave interactions are the likely cause for the simulated supertidal energy at the equator.

To emphasize this point, we plot the ratio of tidal to supertidal energy, following Solano et al. (2023), and $1/\epsilon$, following Wunsch & Marcellino (2023) together in Figure 10. Instead of computing the ratio for the undecomposed fields and the entire supertidal frequency band, we compute the mode-1 ratios for terdiurnal waves,

$$\Upsilon_{1,\mathrm{D3}} = \frac{KE_{1,\mathrm{D3}}}{KE_{1,\mathrm{D1}} + KE_{1,\mathrm{D2}}}, \tag{10}$$

(Figure 10a), and for quarterdiurnal waves,

$$\Upsilon_{1,\mathrm{D4}} = \frac{KE_{1,\mathrm{D4}}}{KE_{1,\mathrm{D1}} + KE_{1,\mathrm{D2}}} \tag{11}$$

(Figure 10b), where the subscripts refer to the mode number and frequency band, respectively. We select mode 1 and the $\mathrm{D_3}$ and $\mathrm{D_4}$ supertidal frequency bands because they contain the most energy (Figure 7). We compute ϵ using the hydrostatic Stürm Liouville equation (1). Because c_n does not depend on ω under this approximation, ϵ reduces to an analytical expression that solely depends on the parent wave characteristics, i.e.,

$$\epsilon = \frac{f^2 - 2k_a k_b c_n^2 + 2\omega_a\omega_b}{[\omega_a + \omega_b]^2}. \tag{12}$$

For the case in which the primary harmonic interacts with itself, i.e., $\omega = \omega_a = \omega_b$, $\epsilon = \frac{3f^2}{4\omega^2}$. This implies that the resonance only depends on f and no longer on the stratification. We compare the KE ratios with hydrostatic $1/\epsilon$ computed for the interaction between M_2 and K_1 (Figure 10c) and the self interaction of M_2 (Figure 10d).

In agreement with large $1/\epsilon$ in Figure 10d, $\Upsilon_{1,\mathrm{D4}}$ is strongly enhanced at the equator ($> 25\%$; Figure 10b), suggesting M_2 wave-wave interactions are strong here. Although D_4 energy is also generated at higher latitudes, e.g., the beams radiating from Tasmania and Georges Bank (Figure 7b), their fraction of the primary tidal energy is much smaller ($< 10\%$). These results are in contrast with $\Upsilon_{1,\mathrm{D3}}$, which is only weakly elevated in the tropics and mainly in the beam extending northward from the French Polynesian Islands ($\sim 10\%$; Figure 10a). There may be two reasons for this difference: 1) D_1 internal tides are mainly generated in the western Pacific (Figure 4a) and 2) hydrostatic $1/\epsilon$ is smaller for M_2+K_1 than for M_2+M_2 interactions (see also Figure 10a,b). While $KE_{1,\mathrm{D3}}$ is largest in the western Pacific near Luzon Strait (Figure 7a), both $\Upsilon_{1,\mathrm{D3}}$ ($< 5\%$) and $1/\epsilon$ (~ 0.17) are rather small here. Despite the small $1/\epsilon$, the near-resonant interaction between the tidal modes is sufficient to generate odd and even harmonics (Figures 6b and 8b).

South of 30°S, $\Upsilon_{1,\mathrm{D3}}$ is enhanced in Figure 10a because non-tidal mesoscale and/or high-frequency near-inertial motions project on the D_3 frequency band (Figure 7a) and D_1 and D_2 internal tide energy is generally small (Figure 3a,e). The May/June simulation period coincides with early southern-hemisphere winter featuring relative large wind-energy input and large eddy kinetic energy south of 30°S (Raja et al., 2022).

The aforementioned theoretical studies and our results imply that tidal internal waves with the same mode number can resonantly (self) interact. However, it follows from eq. (9) that waves with different mode numbers are not inclined to resonantly interact. Hence, it is interesting that Solano et al. (2023) found that when D_2 mode 1 and 2 waves superpose, the cross-frequency energy transfers are enhanced. It could be that the mode 1+2 superposition catalyzes the transfers associated with mode-1 resonant interactions due to the enhanced vertical shear. In future research, we plan to investigate these transfers in detail, preferably with idealized (non)hydrostatic simulations.

4.2.2 Hydrostatic vs. Nonhydrostatic Resonance

In contrast to the nonhydrostatic $1/\epsilon$ map of Wunsch & Marcellino (2023) (their Figure 3), the hydrostatic $1/\epsilon$ values in Figure 10c,d are smooth fields. To elucidate their differences we compute nonhydrostatic $1/\epsilon$ along a meridional transect at 327.92°E in the Atlantic Ocean for interactions between M_2 and K_1, M_2 and M_2, M_2 and M_4, and between M_4 and M_4 for modes 1-3 (Figure 11). Note that all parent and child waves involved in the same interaction have the same mode number. The near-resonant child frequency $\omega_c = \omega(k_a + k_b)$ is computed by linear interpolation from the nonhydrostatic dispersion curve $k_c(\omega_c)$. In addition to f, nonhydrostatic $1/\epsilon$ also depends on the stratification, causing a noisier field. Moreover, pure resonance is no longer obtained as compared to hydrostatic $1/\epsilon$, which tends towards infinity for small f. Compared to hydrostatic $1/\epsilon$, the maximum value of nonhydrostatic $1/\epsilon$ decreases for interactions between parent waves with higher frequencies, i.e., they become less resonant at low latitudes. However, both the hydrostatic and nonhydrostatic $1/\epsilon$ values increase at high latitudes for interactions between parent waves with higher frequencies, i.e., for higher-frequency nonhydrostatic waves the resonance becomes more independent of latitude. Finally, hydrostatic $1/\epsilon$ does not depend on the mode number in contrast to nonhydrostatic $1/\epsilon$. Interestingly, at this particular transect, mode 2 is slightly more resonant than modes 1 and 3 near the equator. For higher latitudes, the differences between the various $1/\epsilon$ curves disappear because of the relative importance of f (e.g., eq. 12).

Does Figure 11 suggest that hydrostatic model simulations feature stronger resonant low-mode wave-wave interactions than nonhydrostatic model simulations? If this is true, then would that result in more pronounced higher harmonics, as shown in Figures 6 and 8 and in several studies on hydrostatic global ocean model simulations (e.g,

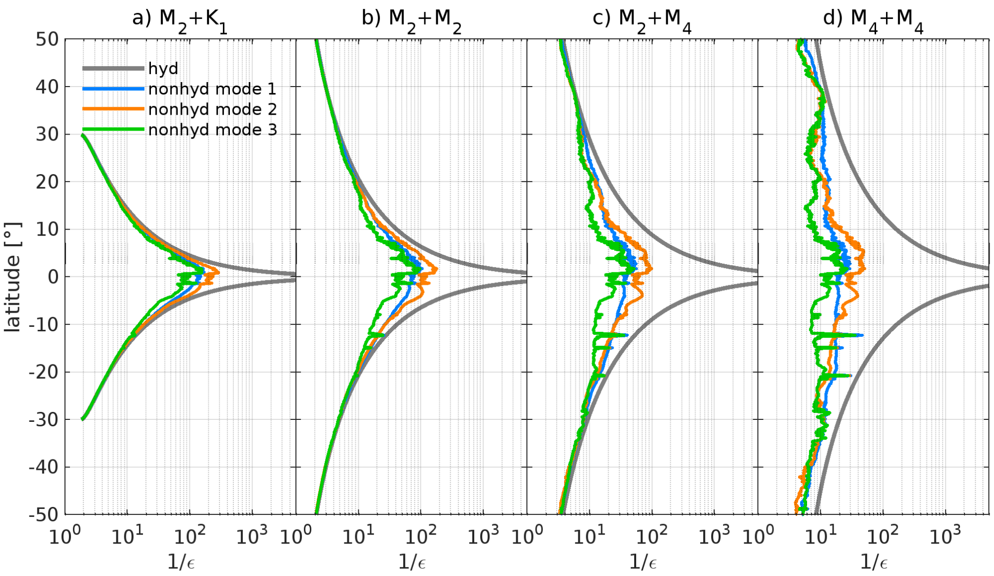

Figure 11. Resonance parameter $1/\epsilon$ for wave-wave interactions between (a) M_2 and K_1, (b) M_2 and M_2, (c) M_2 and M_4, (d) M_4 and M_4 hydrostic ("hyd") and nonhydrostatic ("nonhyd") modes along a meridional transect at 327.92°E in the Atlantic Ocean. All wave pairs have the same mode number. $1/\epsilon$ for the hydrostatic mode pairs all coincide with the thick gray line.

Yu et al., 2019; Arbic et al., 2022; Ansong et al., 2024)? Theoretically, differences between the hydrostatic and nonhydrostatic dispersion relations become apparent for higher frequencies (Figure 8). However, it is difficult to establish from Figure 8 that the hydrostatic dispersion relation agrees better with the simulated $\omega-k$ spectra than the nonhydrostatic dispersion relation (although the hydrostatic mode-1 curve seems to agree better for large k). Potential reasons for this are that eq. (1) is based on the linearized internal wave relations without background flow, changes in parameters along the transect, and numerical dispersion mimics nonhydrostatic dispersion in hydrostatic simulations (Vitousek & Fringer, 2011).

While we cannot address the above question in this paper, other factors may also explain the pronounced higher harmonics in hydrostatic global ocean simulations with horizontal grid-spacings of 2-4 km. These simulations may under-resolve eddy-wave scattering and wave-wave interactions that tend to fill in the valleys between the harmonic spectral peaks and raise the continuum energy levels in higher resolution simulations in agreement with observations (e.g., Luecke et al., 2020; Nelson et al., 2020; Yang et al., 2023; Delpech et al., 2024).

4.3 Decay of Supertidal Modes

An interesting feature of mode-1 supertidal energy fluxes in Figures 4i and 7 is that the beams are well defined and that they extend across the tropics for 1000s of km. For example, the Amazon beams extend to the Iberian Peninsula and northwest Africa. Similarly, the French Polynesian Island beams nearly reach the Baja Peninsula in North America. The semidiurnal mode 1 beams from the respective generation sites in Figure 4e do not appear to extend that far, most likely because they disappear in the mode 1 background noise. There may be several reasons why the HH beams extend that far: this 4-km global HYCOM simulation has lower continuum energy levels (e.g., Luecke et al., 2020; Ansong et al., 2024) that could mask these HH beams in the farfield, the model resolution may not be sufficient to cascade this supertidal energy to smaller temporal and spatial scales, and the vertical shear in these low modes may be too weak to trigger dissipation due to the KPP subgrid scale mixing scheme. Hence, the decay is small and energy is stuck in these low supertidal modes. This behavior may also be reflected in the mode-1 KE, which spectral slopes in Figure 6 are flatter than the higher modes. When energy is "stuck" in a mode, this mode may have more time to interact with itself and contribute to more pronounced higher harmonics.

4.4 Comparison with Observations

Supported by theory (Figure 10c,d), our HYCOM simulation predicts a poleward decrease in the fraction of higher harmonic energy (Figure 10a,b; Solano et al., 2023). However, it is not yet clear from the literature if these spatial patterns exist in observations. Hence, we are currently diagnosing hundreds of historical mooring observations from, o.a., the Global Multi-Archive Current Meter Database (GMACMD; Scott et al., 2011) to quantify the energy in the higher harmonics.

Unfortunately, not many studies exist in which moorings have been placed directly in strong internal tide beams, in particular in the tropics. For example, Xie et al. (2010) present energy spectra of mooring observations in the South China Sea in the westward nonlinear internal tide beam from Luzon Strait (20°N). The spectra in, e.g., their Figure 2 show the same harmonics (D_1-D_{10}) and a similar slope as the mode-1 spectra in Figure 6b. Using bicoherence spectra, they determined that the nonlinear interactions between D_2 and D_2 were stronger than between D_2 and D_1, which would be in agreement with $1/\epsilon$ for M_2+K_1 and M_2+K_2 in Figures 10c,d and 11a,b. However, Xie et al. (2010) suggested that these harmonics were not associated with near-resonant wave-wave interactions. At a higher latitude ($\sim$ 46°N), seaward of the Bay of Biscay shelf slope, van Haren et al. (2002) observed higher harmonics of D_2 in spectra obtained from a current meter moored at 1000 m above the seafloor. van Haren & Maas (2022) attributed these harmonics to non-resonant nonlinear interactions. In both these areas, we simulate propagating higher harmonic wave modes (e.g., see the mode 1 supertidal flux in Figure 4i). Hence, we postulate that the observed harmonics in these studies are attributed to near-resonant wave-wave interactions as discussed in Section 4.2.1.

5 Conclusions

In this study, we diagnose the spatial variability in the energetics of tidally generated diurnal, semidiurnal, and supertidal hydrostatic modes (up to mode 6) in a 30-day forward global HYCOM simulation with a 4-km grid spacing and 41 layers. This simulation is forced with realistic tides and atmospheric fields. We discuss how vertical and horizontal grid spacing affects the resolution of the modes and how the generation of supertidal modes may be attributed to wave-wave interactions. Our key findings are as follows:

- While diurnal modes are mostly generated in the western Pacific, in Luzon Strait and Indonesian archipelago, semidiurnal modes are more ubiquitous in the global ocean. Supertidal modes are mostly generated at low latitudes.
- For all frequency bands, most of the energy is in mode 1. Diurnal modes are fully resolved beyond mode 6, semidiurnal modes are fully resolved up to mode 4, and supertidal modes are fully resolved up to mode 2.
- The meridional trends of $\frac{KE}{APE}$ of the resolved modes agree with the theoretical internal wave consistency relation $\frac{\omega^2+f^2}{\omega^2-f^2}$.
- The supertidal band is dominated by the terdiurnal and quarterdiurnal mode-1 waves. Terdiurnal modes are mostly generated in the west Pacific, where diurnal internal tides are strong. Quarterdiurnal modes occur at all longitudes, but mostly

in the tropics, near strong semidiurnal generation sites. The ratio between supertidal and tidal energy (Υ) is elevated in the tropics.

- The consistency relation and frequency-wavenumber spectra show that the resolved supertidal modes are dispersive internal waves and likely generated by near-resonant interactions between modes of the same mode number. In agreement with simulated Υ, the theoretical resonance parameter ($1/\epsilon$) is also enhanced in the tropics and stronger for M_2+M_2, than for M_2+K_1 (or M_2+O_1) near-resonant interactions.
- The horizontal resolution criterion, which mandates that 6-8 of grid cells per wavelength are required to resolve a mode, reasonably predicts the number of resolved modes for the diurnal, semidiurnal, and supertidal in the tropics. However, we cannot establish a good correlation between the spatial variability in the horizontal and vertical resolution criteria and the simulated resolved modes.

Appendix A Amplitude Error due to Finite Differences

To better understand how the horizontal grid spacing affects the number of resolved wave modes, we consider how finite difference errors of a sinusoidal wave change with respect to horizontal grid spacing. It is likely that errors are further increased when considering time integration and advective terms. Hence, the following analysis is an estimate of the minimum error.

Given a grid of spacing Δx, noting the position at the j^{th} point $x_j = j\Delta x$ and the value of a function at the point $\mathcal{F}(x_j) = \mathcal{F}_j$, we define the second order centered finite difference of a first derivative as

$$\left.\frac{d\mathcal{F}}{dx}\right|_{x_j} = \frac{\mathcal{F}_{j+1} - \mathcal{F}_{j-1}}{2\Delta x} + \epsilon_j, \tag{A1}$$

where ϵ_j is the error involved in the finite difference estimate. Assume the function is only a sinusoid: $\mathcal{F}(x_j) = e^{i(kx_j+\phi)}$, where k is the wavenumber measured in units of radians per unit of x, and ϕ is a phase offset measured in radians. Then the derivative is

$$\left.\frac{d\mathcal{F}}{dx}\right|_{x_j} = \frac{e^{i(k(j+1)\Delta x+\phi)} - e^{i(k(j-1)\Delta x+\phi)}}{2\Delta x} + \epsilon_j, \tag{A2}$$

and the error is

$$\epsilon_j = \frac{e^{i(k(j+1)\Delta x+\phi)} - e^{i(k(j-1)\Delta x+\phi)}}{2\Delta x} - ike^{i(kj\Delta x+\phi)}. \tag{A3}$$

After some algebra, we find

$$\begin{aligned}\epsilon_j &= \frac{e^{ikj\Delta x}(e^{ik\Delta x} - e^{-ik\Delta x})e^{i\phi}}{2\Delta x} - ike^{ikj\Delta x}e^{i\phi} \\ &= e^{ikj\Delta x}e^{i\phi}\left(\frac{e^{ik\Delta x} - e^{-ik\Delta x}}{2\Delta x} - ik\right).\end{aligned} \tag{A4}$$

The amplitude of the error A_{ϵ_j} is a product of three terms, the first two of which are 1. Therefore,

$$\begin{aligned}A_{\epsilon_j} &= \left|\frac{e^{ik\Delta x} - e^{-ik\Delta x}}{2\Delta x} - ik\right| \\ &= \left|\frac{\sin(k\Delta x)}{\Delta x} - k\right|.\end{aligned} \tag{A5}$$

In Figure A1, the amplitude of the error, normalized by the amplitude of the slope function $d(\sin(kx+\phi))/dx$ is plotted vs. the number of grid points per wavelength $\frac{2\pi}{k\Delta x}$. In the limit of $\Delta x \to 0$, the amplitude of the error $A_{\epsilon_j} \to 0$. The normalized amplitude error A_{ϵ_j}/k is about 10% for eight grid cells in a wavelength (Figure A1).

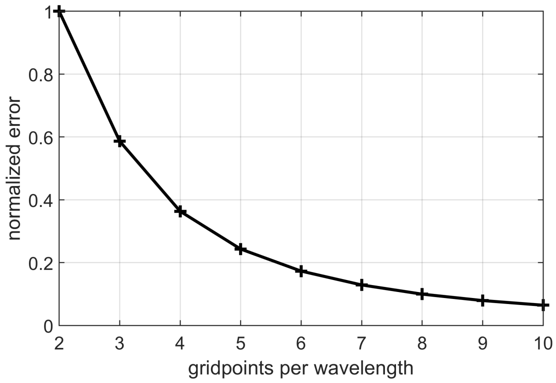

Figure A1. Amplitude error as a function of the number of gridcells per wavelength normalized by the amplitude of $d(\sin(kx))/dx$.

Open Research Section

The raw HYCOM simulation data of ∼40 terabytes (TB) and diagnosed fields are available upon request for those that have access to the United States Department of Defense super computers. The seafloor depth, grid coordinates, eigenspeeds for modes 1-5, and the time-mean kinetic energy and energy fluxes for modes 1-5 for several frequency bands are accessible at Zenodo: `https://doi.org/10.5281/zenodo.7909290`.

Acknowledgments

M. Buijsman and M. Solano are funded by the Office of Naval Research (ONR) grant N00014-19-1-2704. M. Buijsman and D. Varma are funded by the ONR grant N0014-22-1-2576. M. Buijsman is also funded by National Science Foundation (NSF) grant OCE2319143 and National Aeronautics and Space Administration (NASA) grants 80NSSC18K0771, 80NSSC20K1135, and 80NSSC24K1649. J. Shriver acknowledges support from ONR grant N00014-23-WX0-1413. B.K. Arbic acknowledges support from ONR grant N00014-19-1-2712 and NASA grant 80NSSC24K1649. E.P. Chassignet, L. Hiron, and X. Xu acknowledge support from ONR grants N00014-19-1-2717, N00014-20-1-2769, and N00014-22-1-2574 and NASA grants 80NSSC20K1135 and 80NSSC24K1649. M. Abdulfatai is supported by N00014-22-1-2574. We thank Gregg Jacobs of the Naval Research Laboratory for feedback on finite difference amplitude errors.

References

Alford, M. H., & Zhao, Z. (2007). Global patterns of low-mode internal-wave propagation. part i: Energy and energy flux. *Journal of Physical Oceanography*, *37*(7), 1829–1848. doi: 10.1175/JPO3085.1

Aluie, H., Hecht, M., & Vallis, G. K. (2018). Mapping the energy cascade in the North Atlantic Ocean: The coarse-graining approach. *Journal of Physical Oceanography*, *48*(2), 225–244.

Ansong, J. K., Arbic, B. K., Nelson, A. D., Alford, M. H., Kunze, E., Menemenlis, D., ... Buijsman, M. C. (2024). Surface and sub-surface kinetic energy wavenumber-frequency spectra in global ocean models and observations. *Journal of Geophysical Research: Oceans*, *129*(6), e2023JC020480. doi: 10.1029/2023JC020480

Ansong, J. K., Arbic, B. K., Simmons, H. L., Alford, M. H., Buijsman, M. C., Timko, P. G., ... Wallcraft, A. J. (2018). Geographical distribution of diurnal and semidiurnal parametric subharmonic instability in a global ocean circulation model. *Journal of Physical Oceanography*, *48*(6), 1409–1431.

Arbic, B. K. (2022). Incorporating tides and internal gravity waves within global ocean general circulation models: A review. *Progress in Oceanography*, *206*, 102824. doi: 10.1016/j.pocean.2022.102824

Arbic, B. K., Alford, M., Ansong, J., Buijsman, M., Ciotti, R., Farrar, J., ... Zhao, Z. (2018). A primer on global internal tide and internal gravity wave continuum modeling in HYCOM and MITgcm. In E. Chassignet, A. Pascual, J. Tintore, & J. Verron (Eds.), *New frontiers in operational oceanography* (pp. 307–392). GODAE OceanView. doi: 10.17125/gov2018.ch13.

Arbic, B. K., Elipot, S., Brasch, J. M., Menemenlis, D., Ponte, A. L., Shriver, J. F., ... Nelson, A. D. (2022). Near-surface oceanic kinetic energy distributions from drifter observations and numerical models. *Journal of Geophysical Research: Oceans*, *127*(10), e2022JC018551. doi: 10.1029/2022JC018551

Arbic, B. K., Garner, S. T., Hallberg, R. W., & Simmons, H. L. (2004). The accuracy of surface elevations in forward global barotropic and baroclinic tide models. *Deep-Sea Research II*, *51*, 3069-3101.

Baker, L. E., Doak, A., & Bi, D. (2024). Near-resonant generation of internal tide superharmonics in a global ocean model. *ESS Open Archive*. doi: 10.22541/essoar.173524482.28899706/v1

Baker, L. E., & Sutherland, B. R. (2020). The evolution of superharmonics excited by internal tides in non-uniform stratification. *Journal of Fluid Mechanics*, *891*, R1. doi: 10.1017/jfm.2020.188

Barkan, R., Srinivasan, K., & McWilliams, J. C. (2024). Eddy–internal wave interactions: Stimulated cascades in cross-scale kinetic energy and enstrophy fluxes. *Journal of Physical Oceanography*, *54*(6), 1309–1326.

Bell Jr., T. H. (1975). Topographically generated internal waves in the open ocean. *Journal of Geophysical Research (1896-1977)*, *80*(3), 320-327. doi: 10.1029/JC080i003p00320

Bleck, R. (2002). An oceanic general circulation model framed in hybrid isopycnic cartesian coordinates. *Ocean Modelling*, *4*, 55-88.

Buijsman, M. C., Ansong, J., Arbic, B., Richman, J., Shriver, J., Timko, P., ... Zhao, Z. (2016). Impact of parameterized internal wave drag on the semidiurnal energy balance in a global ocean circulation model. *Journal of Physical Oceanogry*, *46*, 1399–1419. doi: 10.1175/JPO-D-15-0074.1

Buijsman, M. C., Kanarska, Y., & McWilliams, J. C. (2010). On the generation and evolution of nonlinear internal waves in the South China Sea. *Journal of Geophysical Research*, *115*. doi: 10.1029/2009JC005275

Buijsman, M. C., Stephenson, G. R., Ansong, J. K., Arbic, B., Green, M., Shriver, J. G. R. J., ... Zhao, Z. (2020). On the interplay between horizontal resolution and wave drag and their effect on tidal baroclinic mode waves in realistic global ocean simulations. *Ocean Modelling*, *152*(101656). doi: 10.1016/j.ocemod.2020.101656

Chassignet, E., Hurlburt, H., Metzger, E., Smedstad, O., Cummings, J., Halliwell, G., ... Wilkin, J. (2009). U.s. godae: Global ocean prediction with the HYbrid Coordinate Ocean Model (HYCOM). *Oceanography*, *22*(2), 64–75.

Chassignet, E., Smith, L., Halliwell, G., & Bleck, R. (2003). North Atlantic simulations with the HYbrid Coordinate Ocean Model (HYCOM): Impact of the vertical coordinate choice, reference density, and thermobaricity. *Journal of Physical Oceanography*, *33*, 2504–2526.

Dauxois, T., Joubaud, S., Odier, P., & Venaille, A. (2018). Instabilities of internal gravity wave beams. *Annual Review of Fluid Mechanics*, *50*, 131–156. doi: https://doi.org/10.1146/annurev-fluid-122316-044539

de Lavergne, C., Falahat, S., Madec, G., Roquet, F., Nycander, J., & Vic, C. (2019).

Toward global maps of internal tide energy sinks. *Ocean Modelling*, *137*, 52-75. doi: 10.1016/j.ocemod.2019.03.010

Delpech, A., Barkan, R., Srinivasan, K., McWilliams, J. C., Arbic, B. K., Siyanbola, O. Q., & Buijsman, M. C. (2024). Eddy–internal wave interactions and their contribution to cross-scale energy fluxes: A case study in the california current. *Journal of Physical Oceanography*, *54*(3), 741–754.

Diamessis, P., Wunsch, S., Delwiche, I., & Richter, M. (2014). Nonlinear generation of harmonics through the interaction of an internal wave beam with a model oceanic pycnocline. *Dynamics of Atmospheres and Oceans*, *66*, 110–137. doi: 10.1016/j.dynatmoce.2014.02.003

Egbert, G. D., & Ray, R. D. (2003). Semi-diurnal and diurnal tidal dissipation from TOPEX/Poseidon altimetry. *Geophysical Research Letters*, *30*. doi: 10.1029/2003GL017676

Farmer, D., Li, Q., & Park, J. (2009). Internal wave observations in the south china sea: The role of rotation and non-linearity. *Atmosphere-Ocean*, *47*, 267-280. doi: 10.3137/OC313.2009

Garrett, C., & Munk, W. (1975). Space-time scales of internal waves: A progress report. *Journal of Geophysical Research (1896-1977)*, *80*(3), 291-297. doi: 10.1029/JC080i003p00291

Gerkema, T. (2001). Internal and interfacial tides: Beam scattering and local generation of solitary waves. *Journal of Marine Research*, *59*, 227–255.

Gerkema, T. (2006). Internal-wave reflection from uniform slopes: higher harmonics and coriolis effects. *Nonlinear Processes in Geophysics*, *13*(3), 265–273. doi: 10.5194/npg-13-265-2006

Gerkema, T., & Zimmerman, J. T. F. (1995). Generation of nonlinear internal tides and solitary waves. *Journal of Physical Oceanography*, *25*(6), 1081–1094. doi: 10.1175/1520-0485(1995)025⟨1081:GONITA⟩2.0.CO;2

Gill, A. E. (1982). *Atmosphere-ocean dynamics* (Vol. 30). Academic Press.

Gong, Y., Rayson, M. D., Jones, N. L., & Ivey, G. N. (2021). Directional decomposition of internal tides propagating from multiple generation sites. *Ocean Modelling*, *162*. doi: 10.1016/j.ocemod.2021.101801

Grisouard, N., Staquet, C., & Gerkema, T. (2011). Generation of internal solitary waves in a pycnocline by an internal wave beam: a numerical study. *Journal of Fluid Mechanics*, *676*, 491–513. doi: 10.1017/jfm.2011.61

Hallberg, R. (2013). Using a resolution function to regulate parameterizations of oceanic mesoscale eddy effects. *Ocean Modelling*, *72*, 92–103. doi: 10.1016/j.ocemod.2013.08.007

Hazewinkel, J., & Winters, K. (2011). Psi of the internal tide on a β plane: flux divergence and near-inertial wave propagation. *Journal of Physical Oceanography*, *41*(9), 1673–1682.

Hiron, L., Schönau, M. C., Raja, K. J., Chassignet, E. P., Buijsman, M. C., Arbic, B. K., . . . Solano, M. (2024). *The influence of vertical resolution on internal tide energetics and subsequent effects on underwater acoustic propagation.* Retrieved from `https://arxiv.org/abs/2404.05924`

Kang, D., & Fringer, O. (2010). On the calculation of available potential energy in internal wave fields. *Journal of Physical Oceanography*, *40*(11), 2539–2545. doi: 10.1175/2010JPO4497.1

Kelly, S. M. (2016). The vertical mode decomposition of surface and internal tides in the presence of a free surface and arbitrary topography. *Journal of Physical Oceanography*, *46*, 3777–3788. doi: 10.1175/JPO-D-16-0131.1

Kelly, S. M., & Lermusiaux, P. F. (2016). Internal-tide interactions with the gulf stream and middle atlantic bight shelfbreak front. *Journal of Geophysical Research: Oceans*, *121*. doi: 10.1002/2016JC011639

Kelly, S. M., Nash, J. D., Martini, K. I., Alford, M. H., & Kunze, E. (2012). The cascade of tidal energy from low to high modes on a continental slope. *Journal of physical oceanography*, *42*(7), 1217–1232.

Kelly, S. M., Waterhouse, A. F., & Savage, A. C. (2021). Global dynamics of the stationary m2 mode-1 internal tide. *Geophysical Research Letters*, *48*. doi: 10.1029/2020GL091692

Kunze, E. (2017). Internal-wave-driven mixing: Global geography and budgets. *Journal of Physical Oceanography*, *47*, 1325–1345. doi: 10.1175/JPO-D-16-0141.1

Lamb, K. G. (2007). Tidally generated near-resonant internal wave triads at a shelf break. *Geophysical Research Letters*, *34*(18). doi: 10.1029/2007GL030825

Li, Z., & von Storch, J.-S. (2020). M2 internal-tide generation in stormtide2. *Journal of Geophysical Research: Oceans*, *125*(8), e2019JC015453. doi: 10.1029/2019JC015453

Luecke, C. A., Arbic, B. K., Richman, J. G., Shriver, J. F., Alford, M. H., Ansong, J. K., … Zamudio, L. (2020). Statistical comparisons of temperature variance and kinetic energy in global ocean models and observations: Results from mesoscale to internal wave frequencies. *Journal of Geophysical Research Oceans*, *125*(5), e2019JC015306. doi: 10.1029/2019JC015306

Müller, M., Arbic, B., Richman, J., Shriver, J., Kunze, E., Scott, R. B., … Zamudio, L. (2015). Toward an internal gravity wave spectrum in global ocean models. *Geophysical Research Letters*, *42*, 3474–3481. doi: 10.1002/2015GL063365

Müller, M., Cherniawsky, J., Foreman, M., & von Storch, J. (2012). Global M_2 internal tide and its seasonal variability from high resolution ocean circulation and tide modeling. *Geophysical Research Letters*, *39*, L19607.

Nelson, A. D., Arbic, B. K., Menemenlis, D., Peltier, W. R., Alford, M. H., Grisouard, N., & Klymak, J. M. (2020). Improved internal wave spectral continuum in a regional ocean model. *Journal of Geophysical Research: Oceans*, *125*(5), e2019JC015974. doi: 10.1029/2019JC015974

Ngodock, H. E., Souopgui, I., Wallcraft, A. J., Richman, J. G., Shriver, J. F., & Arbic, B. K. (2016). On improving the accuracy of the m_2 barotropic tides embedded in a high-resolution global ocean circulation model. *Ocean Modelling*, *97*, 16–26. doi: 10.1016/j.ocemod.2015.10.011

Pan, Y., Haley, P. J., & Lermusiaux, P. F. (2021). Interactions of internal tides with a heterogeneous and rotational ocean. *Journal of Fluid Mechanics*, *920*, A18. doi: 10.1017/jfm.2021.423

Pichon, A., Morel, Y., Baraille, R., & Quaresma, L. S. (2013). Internal tide interactions in the bay of biscay: Observations and modelling. *Journal of Marine Systems*, *109–110*, S26–S44. doi: 10.1016/j.jmarsys.2011.07.003

Raja, K. J., Buijsman, M. C., Bozec, A., Helber, R. W., Shriver, J. F., Wallcraft, A., … Arbic, B. K. (2024). Spurious internal wave generation during data assimilation in eddy resolving ocean model simulations. *Ocean Modelling*, *188*, 102340. doi: 10.1016/j.ocemod.2024.102340

Raja, K. J., Buijsman, M. C., Shriver, J. F., Arbic, B. K., & Siyanbola", O. (2022). Near-inertial wave energetics modulated by background flows in a global model simulation. *Journal of physical oceanography*, *52*(5), 823–840. doi: 10.1175/JPO-D-21-0130.1

Rocha, C. B., Gille, S. T., Chereskin, T. K., & Menemenlis, D. (2016). Seasonality of submesoscale dynamics in the kuroshio extension. *Geophysical Research Letters*, *43*(21), 11304–11311. doi: 10.1002/2016GL071349

Savage, A. C., Arbic, B. K., Alford, M. H., Ansong, J. K., Farrar, J. T., Menemenlis, D., … Zamudio, L. (2017). Spectral decomposition of internal gravity wave sea surface height in global models. *Journal of Geophysical Research: Oceans*, *122*(10), 7803-7821. doi: 10.1002/2017JC013009

Scott, R. B., Goff, J. A., Naveira Garabato, A. C., & Nurser, A. J. G. (2011). Global rate and spectral characteristics of internal gravity wave generation by geostrophic flow over topography. *Journal of Geophysical Research: Oceans*, *116*(C9). doi: 10.1029/2011JC007005

Shriver, J. F., Arbic, B. K., Richman, J. G., Ray, R. D., Metzger, E. J., Wallcraft, A. J., & Timko, P. G. (2012). An evaluation of the barotropic and internal tides in a high resolution global ocean circulation model. *Journal of Geophysical Research: Oceans*, *117*. doi: 10.1029/2012JC008170

Simmons, H. L., & Alford, M. H. (2012). Simulating the long-range swell of internal waves generated by ocean storms. *Oceanography*, *25*, 30–41. Retrieved from `https://doi.org/10.5670/oceanog.2012.39`

Simmons, H. L., Hallberg, R. W., & Arbic, B. K. (2004). Internal wave generation in a global baroclinic tide model. *Deep-Sea Research II*, *51*, 3043-3068.

Siyanbola, O. Q., Buijsman, M. C., Delpech, A., Barkan, R., Pan, Y., & Arbic, B. K. (2024). Interactions of remotely generated internal tides with the u.s. west coast continental margin. *Journal of Geophysical Research: Oceans*, *129*(6), e2023JC020859. doi: 10.1029/2023JC020859

Skitka, J., Arbic, B. K., Thakur, R., Menemenlis, D., Peltier, W. R., Pan, Y., ... Ma, Y. (2024). Probing the nonlinear interactions of supertidal internal waves using a high-resolution regional ocean model. *Journal of Physical Oceanography*, *54*(2), 399 - 425. doi: https://10.1175/JPO-D-22-0236.1

Solano, M., Buijsman, M. C., Shriver, J., Magalhaes, J., da Silva, J. C. B., Jackson, C., ... Barkan, R. (2023). Nonlinear internal tides in a realistically forced global ocean simulation. *Journal of Geophysical Research*, *128*. doi: 10.1029/2023JC019913

Stewart, K. D., Hogg, A. M. C., Griffies, S. M., Heerdegen, A. P., Ward, M. L., Spence, P., & England, M. H. (2017). Vertical resolution of baroclinic modes in global ocean models. *Ocean Modelling*, *113*, 50–65. doi: 10.1016/j.ocemod.2017.03.012

Sutherland, B. R. (2016). Excitation of superharmonics by internal modes in non-uniformly stratified fluid. *Journal of Fluid Mechanics*, *793*, 335–352. doi: 10.1017/jfm.2016.108

Sutherland, B. R., & Dhaliwal, M. S. (2022). The nonlinear evolution of internal tides. part 1: the superharmonic cascade. *Journal of Fluid Mechanics*, *948*, A21. doi: 10.1017/jfm.2022.689

Tabaei, A., Akylas, T. R., & Lamb, K. G. (2005). Nonlinear effects in reflecting and colliding internal wave beams. *Journal of Fluid Mechanics*, *526*, 217–243. doi: 10.1017/s0022112004002769

Tchilibou, M., Koch-Larrouy, A., Barbot, S., Lyard, F., Morel, Y., Jouanno, J., & Morrow, R. (2022). Internal tides off the amazon shelf during two contrasted seasons : Interactions with background circulation and ssh imprints. *Ocean Science Discussions*. doi: 10.5194/os-2021-114

Thorpe, S. A. (1966). On wave interactions in a stratified fluid. *Journal of Fluid Mechanics*, *24*(4), 737–751. doi: 10.1017/S002211206600096X

van Aken, H. M., van Haren, H., & Maas, L. R. M. (2007). The high-resolution vertical structure of internal tides and near-inertial waves measured with an adcp over the continental slope in the bay of biscay. *Deep-Sea Research Part I: Oceanographic Research Papers*, *54*, 533–556. doi: 10.1016/j.dsr.2007.01.003

van Haren, H., & Maas, L. (2022). *A simple model for an internal wave spectrum dominated by non-linear interactions.* arXiv. doi: 10.48550/ARXIV.2203.00475

van Haren, H., Maas, L., & van Aken, H. (2002). On the nature of internal wave spectra near a continental slope. *Geophysical Research Letters*, *29*. doi: 10.1029/2001gl014341

Varma, D., Chalamalla, V. K., & Mathur, M. (2020). Spontaneous superharmonic internal wave excitation by modal interactions in uniform and nonuniform stratifications. *Dynamics of Atmospheres and Oceans*, *91*, 101159. doi: 10.1016/j.dynatmoce.2020.101159

Varma, D., & Mathur, M. (2017). Internal wave resonant triads in finite-depth non-uniform stratifications. *Journal of Fluid Mechanics*, *824*, 286–311. doi: 10.1017/jfm.2017.343

Vic, C., Naveira-Garabato, A., Green, J., Waterhouse, A., Zhao, Z., Melet, A., ... Stephenson, G. (2019). Deep-ocean mixing driven by small-scale internal tides. *Nature Communications*, *10*(2099). doi: 10.1038/s41467-019-10149-5

Vitousek, S., & Fringer, O. B. (2011). Physical vs. numerical dispersion in nonhydrostatic ocean modeling. *Ocean Modelling*, *40*, 72–86. doi: 10.1016/j.ocemod.2011.07.002

Wunsch, S. (2017). Harmonic generation by nonlinear self-interaction of a single internal wave mode. *Journal of Fluid Mechanics*, *828*, 630–647. doi: 10.1017/jfm.2017.532

Wunsch, S., & Marcellino, F. J. (2023). Estimates of mode-1 internal tide harmonic generation in the global ocean. *Phys. Rev. Fluids*, *8*, 124801. doi: 10.1103/PhysRevFluids.8.124801

Xie, X., Shang, X., & Chen, G. (2010). Nonlinear interactions among internal tidal waves in the northeastern south china sea. *Chin. J. Ocean. Limnol.*, *28*, 996–1001. doi: 10.1007/s00343-010-9064-8

Xu, X., Chassignet, E. P., & Wallcraft, A. (2023). Impact of vertical resolution on representing baroclinic modes and water mass distribution in the north atlantic circulation. *submitted to Ocean Modelling*.

Xu, X., Chassignet, E. P., Wallcraft, A. J., Arbic, B. K., Buijsman, M. C., & Solano, M. (2022). On the spatial variability of the mesoscale sea surface height wavenumber spectra in the atlantic ocean. *Journal of Geophysical Research: Oceans*, *127*(10), e2022JC018769. doi: 10.1029/2022JC018769

Yang, L., Barkan, R., Srinivasan, K., McWilliams, J. C., Shakespear, C. J., & Gibson, A. H. (2023). Oceanic eddies induce a rapid formation of an internal wave continuum. *Communications Earth and Environment*, *4*(484). doi: 10.1038/s43247-023-01137-1

Yu, X., Ponte, A. L., Elipot, S., Menemenlis, D., Zaron, E. D., & Abernathey, R. (2019). Surface kinetic energy distributions in the global oceans from a high-resolution numerical model and surface drifter observations. *Geophysical Research Letters*, *46*(16), 9757-9766. doi: 10.1029/2019GL083074

Zhao, Z., Alford, M., Girton, J., Rainville, L., & Simmons, H. (2016). Global observations of open-ocean mode-1 M_2 internal tides. *Journal of Physical Oceanography*, *46*, 1657–1684.

Zilberman, N. V., Becker, J. M., Merrifield, M. A., & Carter, G. S. (2009). Model estimates of M_2 internal tide generation over Mid-Atlantic Ridge topography. *Journal of Physical Oceanography*, *39*, 2635–2651.